

# Photoproduction of $\Xi$ off nucleons

K. Nakayama,<sup>1,2,\*</sup> Yongseok Oh,<sup>1,†</sup> and H. Haberzettl<sup>3,‡</sup>

<sup>1</sup>*Department of Physics and Astronomy, University of Georgia, Athens, GA 30602, USA*

<sup>2</sup>*Institut für Kernphysik, Forschungszentrum Jülich, D-52425 Jülich, Germany*

<sup>3</sup>*Center for Nuclear Studies, Department of Physics,*

*The George Washington University, Washington, DC 20052, USA*

(Dated:)

The photoproduction reaction  $\gamma N \rightarrow KK\Xi$  is investigated based on a relativistic meson-exchange model of hadronic interactions. The production amplitude is calculated in the tree-level approximation from relevant effective Lagrangians, whose (coupling constant) parameters are mostly fixed from the empirical data and/or quark models together with SU(3) symmetry considerations. Gauge invariance of the resulting amplitude is maintained by introducing the contact currents by extending the gauge-invariant approach of Haberzettl for one-meson photoproduction to two-meson photoproduction. The role of the intermediate low-lying hyperons and of the intermediate higher-mass hyperon resonances are analyzed in detail. In particular, the basic features of the production of  $\Xi^-(1318)$  in  $\gamma p \rightarrow K^+K^+\Xi^-$  and their possible manifestations in the forthcoming experimental data are discussed.

PACS numbers: 25.20.Lj, 13.60.Le, 13.60.Rj

## I. INTRODUCTION

In principle, flavor SU(3) symmetry allows for the existence of as many  $\Xi$  resonances as the number of  $N^*$  and  $\Delta^*$  resonances combined [1]. Despite this fact, not much is known about these resonances. Indeed, only a dozen or so  $\Xi$  have been identified so far; among them, only two,  $\Xi(1318)$  and  $\Xi(1530)$ , have four-star status [2]. One of the reasons for this situation is that  $\Xi$  hyperons, being particles with strangeness  $S = -2$ , are difficult to produce having relatively small production rates; they can only be produced via indirect processes from the nucleon. The production of  $\Xi$  baryons were, so far, restricted mainly through the  $K^-p$  reactions [3] or the  $\Sigma$ -hyperon induced reactions [4]. However, since the late 1980's, no significant progress has been made in cascade spectroscopy due to the closing of the then existing kaon factories. Recently, the CLAS Collaboration at the Thomas Jefferson National Accelerator Facility (JLab) has initiated a cascade-physics program [5, 6]; the collaboration, in particular, has established the feasibility to do cascade baryon spectroscopy via photoproduction reactions like  $\gamma p \rightarrow K^+K^+\Xi^-$  and  $\gamma p \rightarrow K^+K^+\pi^-\Xi^0$  [6, 7].<sup>1</sup> A dedicated experiment for these reactions is currently underway; preliminary total cross section data for the first reaction have already been reported [9]. Also, cascade physics has recently received a special interest in connection with the search for the exotic pentaquark states. In fact, the NA49 Collaboration [10] has reported seeing a signal for the pentaquark cascade  $\Xi_5^{--}$ . However, to

date, other experiments with much higher statistics have obtained negative results [11].

To our knowledge, the only theoretical investigation of cascade photoproduction off nucleons is that of Ref. [12], which was devoted to the production of the pentaquark  $\Xi_5$  hyperon. It is extremely timely, therefore, to study this reaction theoretically in the energy range covered at JLab. In the present work we investigate the  $\gamma N \rightarrow KK\Xi$  reaction for incident photon energies up to about 5 GeV. Our approach is based on a relativistic meson-exchange model of hadronic interactions. The reaction amplitude is calculated in the tree-level approximation considering the production mechanisms displayed in Fig. 1, which involve excitation of baryon resonances in the intermediate states. In fact, the Particle Data Group (PDG) [2] quotes a number of four- and three-star  $\Lambda$  and  $\Sigma$  hyperons which may contribute to the production of  $\Xi$  in the present reaction. The  $t$ -channel meson-exchange processes with subsequent decay of the emitted meson into two kaons (meson-production processes) are suppressed in the present reaction, since the produced meson should be exotic having strangeness  $S = +2$ . In addition, the  $t$ -channel meson-exchange processes for  $\bar{K}N \rightarrow K\Xi$  are also suppressed since these can occur only via an exchange of an exotic meson with  $S = +2$ . This means that, to lowest order, the production of a cascade hyperon involves necessarily an excitation of hyperons as shown in Fig. 1. This is quite different from the case of the  $\gamma N \rightarrow K\bar{K}N$  reaction, which has large contributions from vector-meson production processes [13]. Therefore, cascade photoproduction off nucleons should offer also a possibility to extract information on the hyperons with  $S = -1$ .

In this work, we investigate the photoproduction reactions of the ground-state cascade  $\Xi(1318)$ . We will

\*Electronic address: nakayama@uga.edu

†Electronic address: yoh@physast.uga.edu

‡Electronic address: helmut@gwu.edu

<sup>1</sup> An earlier experiment on inclusive  $\Xi$  photoproduction is reported in Ref. [8].

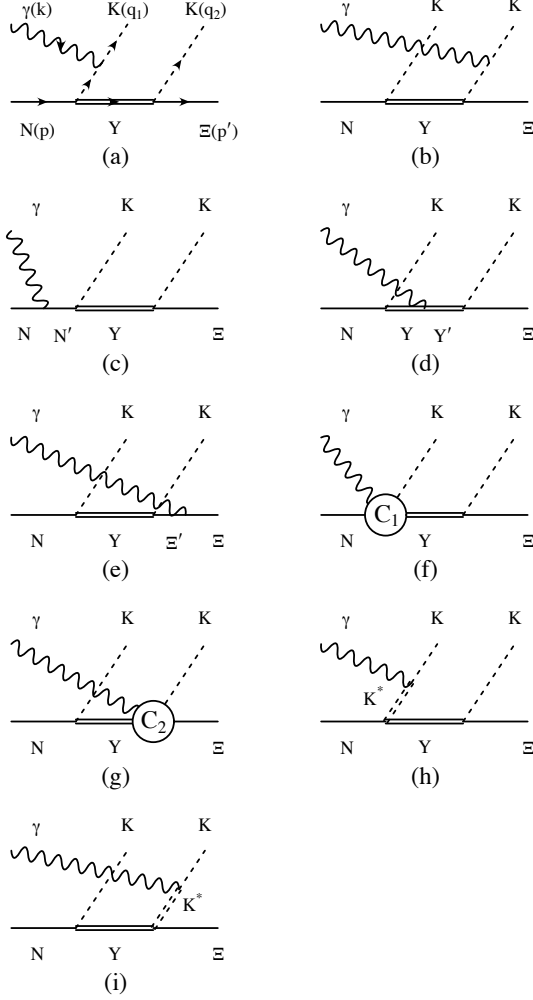


FIG. 1: Diagrams contributing to  $\gamma N \rightarrow K K \Xi$ . The intermediate baryon states are denoted as  $N'$  for the nucleon and  $\Delta$ ,  $Y$ ,  $Y'$  for the hyperon  $\Lambda$  and  $\Sigma$  resonances, and  $\Xi'$  for  $\Xi(1318)$  and  $\Xi(1530)$ . The intermediate mesons in the  $t$ -channel are  $K$  [(a) and (b)] and  $K^*$  [(h) and (i)]. The diagrams (f) and (g) are the generalized contact currents required to maintain gauge invariance of the total amplitude. The off-shell interaction currents corresponding to the diagram parts  $C_1$  and  $C_2$ , respectively, are given in Eqs. (A.22) and (A.25). The external legs are labeled by the four-momenta of the respective particles in (a). Diagrams corresponding to (a)–(i) with  $K(q_1) \leftrightarrow K(q_2)$  are also taken into account in the present calculation.

discuss four different isospin channels, namely,

$$\begin{aligned} \gamma p &\rightarrow K^+ K^+ \Xi^-, & \gamma p &\rightarrow K^+ K^0 \Xi^0, \\ \gamma n &\rightarrow K^+ K^0 \Xi^-, & \gamma n &\rightarrow K^0 K^0 \Xi^0. \end{aligned} \quad (1)$$

At this point, we note that many issues, such as the  $K\Xi$  final-state interaction (FSI), the roles of many of the high-mass nucleon and hyperon resonances, and high-mass vector and axial-vector mesons cannot be addressed

at this stage of the investigation due to a complete lack of independent information as to the dynamics of how these hadrons enter the present reaction.<sup>2</sup> To avoid any speculation on our part, we leave these issues until such time when a better understanding of the underlying reaction dynamics is available. Hence, it is the purpose of the present work to investigate the  $\Xi$  photoproduction mechanism using only the currently available information.

In the next Section, we develop our model for  $\Xi$  photoproduction, which is shown in Fig. 1. We present our results for cross sections and some spin asymmetries in Sec. III. The different role of the intermediate hyperons will be discussed in detail before we summarize in Sec. IV. The effective Lagrangians used in the present work and the method to maintain the gauge-invariance condition with form factors are given in Appendix.

## II. MODEL FOR $\gamma N \rightarrow K K \Xi$

In the present work, the reaction  $\gamma N \rightarrow K K \Xi$  is described by the sum of the amplitudes shown in Fig. 1. The three- and four-star hyperons which may contribute to the present reaction are summarized in Table I. Among them, only for the low-mass resonances, i.e.,  $\Lambda(1116)$ ,  $\Lambda(1405)$ ,  $\Lambda(1520)$ ,  $\Sigma(1190)$ , and  $\Sigma(1385)$ , we have sufficient information to determine the relevant hadronic and electromagnetic coupling constants. In fact, they can be estimated from the experimental data [2] and/or from quark models and SU(3) symmetry considerations. Tables II and III summarize the hyperon resonance parameters and the corresponding estimated coupling constants.

Unfortunately, for higher-mass resonances (those in Table I with a mass larger than 1.6 GeV), there is not sufficient information to extract the necessary parameters, especially their coupling constants to the cascade baryon. The only available information relevant to the present reaction involving the higher hyperon resonances are the  $Y \rightarrow N \bar{K}$  partial decay widths [2], from which we can extract the magnitude of the corresponding  $NYK$  coupling constants. They are displayed in Table I. Therefore, we consider only the diagrams (a)–(g) in Fig. 1 with  $Y = Y'$  in (d), where the only additional parameter is the  $\Xi Y K$  coupling constant. Also, in the following, we will restrict ourselves to spin-1/2 and -3/2 hyperons. It then happens that, unless the  $\Xi Y K$  coupling constants are much larger than the corresponding  $NYK$  coupling constants, resonances with  $J^P = 1/2^+$  and  $3/2^-$  yield much smaller contributions to the reaction amplitude as compared to the  $J^P = 1/2^-$  and  $3/2^+$  resonance contributions. This

<sup>2</sup> The scalar meson exchange, however, is not present in this reaction since the scalar meson cannot couple to the photon and the pseudoscalar meson because of angular-momentum and parity conservation.

TABLE I:  $\Lambda$  and  $\Sigma$  hyperons listed by the Particle Data Group [2] as three-star or four-star states. The decay widths and branching ratios of high-mass resonances  $m_Y > 1.6$  GeV are in a broad range. The coupling constants are determined from their central values.

$\Lambda$ states					$\Sigma$ states				
State	$J^P$	$\Gamma$ (MeV)	Rating	$ g_{N\Lambda K} $	State	$J^P$	$\Gamma$ (MeV)	Rating	$ g_{N\Sigma K} $
$\Lambda(1116)$	$1/2^+$		****		$\Sigma(1193)$	$1/2^+$		****	
$\Lambda(1405)$	$1/2^-$	$\approx 50$	****		$\Sigma(1385)$	$3/2^+$	$\approx 37$	****	
$\Lambda(1520)$	$3/2^-$	$\approx 16$	****						
$\Lambda(1600)$	$1/2^+$	$\approx 150$	***	4.2	$\Sigma(1660)$	$1/2^+$	$\approx 100$	***	2.5
$\Lambda(1670)$	$1/2^-$	$\approx 35$	****	0.3	$\Sigma(1670)$	$3/2^-$	$\approx 60$	****	2.8
$\Lambda(1690)$	$3/2^-$	$\approx 60$	****	4.0	$\Sigma(1750)$	$1/2^-$	$\approx 90$	***	0.5
$\Lambda(1800)$	$1/2^-$	$\approx 300$	***	1.0	$\Sigma(1775)$	$5/2^-$	$\approx 120$	****	
$\Lambda(1810)$	$1/2^+$	$\approx 150$	***	2.8	$\Sigma(1915)$	$5/2^+$	$\approx 120$	****	
$\Lambda(1820)$	$5/2^+$	$\approx 80$	****		$\Sigma(1940)$	$3/2^-$	$\approx 220$	***	$< 2.8$
$\Lambda(1830)$	$5/2^-$	$\approx 95$	****		$\Sigma(2030)$	$7/2^+$	$\approx 180$	****	
$\Lambda(1890)$	$3/2^+$	$\approx 100$	****	0.8	$\Sigma(2250)$	$?^?$	$\approx 100$	***	
$\Lambda(2100)$	$7/2^-$	$\approx 200$	****						
$\Lambda(2110)$	$5/2^+$	$\approx 200$	***						
$\Lambda(2350)$	$9/2^+$	$\approx 150$	***						

can be understood if we consider the limit of the intermediate hyperon resonances being on the mass shell. Then, the photoproduction amplitude becomes proportional to either the sum of the baryon masses or their difference depending on the spin-parity of the resonance, namely,

$$\begin{aligned} M_{1/2^\pm} &\propto (m_Y \mp m_N)(m_Y \mp m_\Xi), \\ M_{3/2^\pm} &\propto (m_Y \pm m_N)(m_Y \pm m_\Xi), \end{aligned} \quad (2)$$

where  $M_{JP}$  denotes the photoproduction amplitude involving the intermediate hyperon with the spin-parity  $J^P$ . Of course, this argument does not quite apply to low-mass resonances which are far off-shell in the present reaction. Among the  $J^P = 1/2^-$  and  $3/2^+$  resonances, assuming the  $\Xi Y K$  coupling strength to be of the order of the  $NYK$  coupling strength, we find that only the  $\Lambda(1800)1/2^-$  and  $\Lambda(1890)3/2^+$  resonances contribute significantly.<sup>3</sup> We, therefore, consider only these two higher-mass resonances in the present exploratory investigation instead of including all hyperon resonances listed in Table I. As such, these two  $\Lambda$  resonances may be viewed as representatives of the spin-1/2 and -3/2 resonances, respectively, in the region of 1.8–2.0 GeV; they are employed here to indicate what features spin-1/2 and -3/2 resonances may introduce into the present reaction.

The interaction Lagrangians for constructing our model for the production amplitudes shown in Fig. 1 are

given in Appendix. The corresponding parameter values are in Tables II and III.

Before presenting our results, we mention that the free parameters in the present model calculation include:

- The pseudoscalar-pseudovector (ps-pv) mixing parameter  $\lambda$  in the meson-baryon ( $BYK$ ) vertex for spin-1/2 baryons  $B$  and  $Y$  in Eq. (A.2). Note that, in principle, because of the Goldstone-boson nature of kaons, chiral symmetry demands the pseudovector-coupling ( $\lambda = 0$ ) choice at least for energies near the threshold. (Strictly speaking, of course, chiral symmetry holds only in the massless kaon limit.) Nevertheless, here we consider both the extreme possibilities:  $\lambda = 0$  and  $\lambda = 1$ .
- The signs of the hadronic and electromagnetic transition coupling constants,  $g_{B\Lambda K} = \pm 0.91$  for  $\Lambda(1405)$  (Table II), and  $g_{\Lambda\Lambda'\gamma} = \pm 1.26$  and  $g_{\Sigma\Lambda'\gamma} = \pm 2.22$  for the transitions  $\Lambda(1116) \leftrightarrow \Lambda(1520)$  and  $\Sigma(1193) \leftrightarrow \Lambda(1520)$ , respectively (Table III). The phases of those coupling constants are not uniquely fixed yet.<sup>4</sup>
- The cutoff parameter  $\Lambda_B$  and the exponent  $n$  in the baryonic form factor in Eq. (A.20). We take these parameters to be the same for all the intermediate baryons.
- The product of the coupling constants,  $g_{N\Lambda K}g_{\Xi\Lambda K}$ ,

<sup>3</sup> Among the  $\Sigma$  resonances, the only candidate is  $\Sigma(1750)$  with  $J^P = 1/2^-$ , which, however, has a very small coupling constant  $g_{N\Sigma K}$ . For  $\Lambda$  resonances, one can expect  $|g_{\Xi\Lambda K}/g_{N\Lambda K}| \leq 1$  since  $g_{\Xi\Lambda K} = g_{N\Lambda K}$  for a singlet  $\Lambda$  and  $g_{\Xi\Lambda K}/g_{N\Lambda K} = (1 - 4f)/(1 + 2f)$  for an octet  $\Lambda$  [14], which is less than 1 for  $0 < f < 1$ .

<sup>4</sup> For those diagrams in Fig. 1 containing the  $NYK$  and  $\Xi Y'K$  vertices with  $Y = Y'$ , their corresponding total phases can be fixed by SU(3) flavor symmetry.

TABLE II: Model parameters employed in the present calculation. The last column cites the sources for the respective values, where PDG refers to Ref. [2].

Nucleon :		
$m_N$ (MeV)	938.3	PDG
$\kappa_{p\gamma}, \kappa_{n\gamma}$	1.79, -1.91	
$\Xi(1318)$ :		
$m_\Xi$ (MeV)	1318.0	
$\kappa_{\Xi^0\gamma}, \kappa_{\Xi^-\gamma}$	-1.25, 0.35	PDG
$\Xi^* [= \Xi(1530)]$ :		
$m_{\Xi^*} (\Gamma_{\Xi^*})$ (MeV)	1533.0 (9.5)	PDG
$\Lambda(1116)$ :		
$m_\Lambda$ (MeV)	1115.7	PDG
$g_{N\Lambda K}$	-13.24	SU(3) + ( $f/d = 0.575$ and $g_{NN\pi} = 13.26$ )
$g_{\Xi\Lambda K}$	3.52	SU(3) + ( $f/d = 0.575$ and $g_{NN\pi} = 13.26$ )
$g_{\Xi^*\Lambda K}$	5.58	SU(3) + ( $f_{N\Delta\pi} = 2.23$ )
$g_{N\Lambda K^*} (\kappa_{N\Lambda K^*})$	-6.11 (2.43)	Ref. [15] (version NSC97f)
$g_{\Xi\Lambda K^*} (\kappa_{\Xi\Lambda K^*})$	6.11 (0.65)	Ref. [15] (version NSC97f)
$\kappa_{\Lambda\gamma}$	-0.613	PDG
$\Lambda(1405)$ :		
$m_\Lambda (\Gamma_\Lambda)$ (MeV)	1406.0 (50.0)	PDG
$g_{N\Lambda K}$	$\pm 0.91$	SU(3) (flavor-singlet assumptions)
$g_{\Xi\Lambda K}$	$\pm 0.91$	SU(3) (flavor-singlet assumptions)
$\kappa_{\Lambda\gamma}$	0.25	Skyrme model [16], unitarized ChPT [17]
$\Sigma(1193)$ :		
$m_\Sigma$ (MeV)	1193.0	PDG
$g_{N\Sigma K}$	3.58	SU(3) + ( $f/d = 0.575$ and $g_{NN\pi} = 13.26$ )
$g_{\Xi\Sigma K}$	-13.26	SU(3) + ( $f/d = 0.575$ and $g_{NN\pi} = 13.26$ )
$g_{\Xi^*\Sigma K}$	3.22	SU(3) + ( $f_{N\Delta\pi} = 2.23$ )
$g_{N\Sigma K^*} (\kappa_{N\Sigma K^*})$	-3.52 (-1.14)	Ref. [15] (version NSC97f)
$g_{\Xi\Sigma K^*} (\kappa_{\Xi\Sigma K^*})$	-3.52 (4.22)	Ref. [15] (version NSC97f)
$\kappa_{\Sigma^+\gamma}, \kappa_{\Sigma^0\gamma}, \kappa_{\Sigma^-\gamma}$	1.46, 0.65, -0.16	PDG
$\Lambda(1520)$ :		
$m_\Lambda (\Gamma_\Lambda)$ (MeV)	1519.5 (15.6)	PDG
$g_{N\Lambda K}$	-10.90	PDG, SU(3) (flavor-octet assumption)
$g_{\Xi\Lambda K}$	3.27	PDG, SU(3) (flavor-octet assumption)
$\kappa_{\Lambda\gamma}$	0.0	assumption
$\Sigma(1385)$ :		
$m_\Sigma (\Gamma_\Sigma)$ (MeV)	1384.0 (37.0)	PDG
$g_{N\Sigma K}$	-3.22	SU(3) + ( $f_{N\Delta\pi} = 2.23$ )
$g_{\Xi\Sigma K}$	-3.22	SU(3) + ( $f_{N\Delta\pi} = 2.23$ )
$f_{\Xi^*\Sigma K}$	-2.83	SU(3) + ( $f_{\Delta\Delta\pi} = 0.8$ from quark model)
$g_{N\Sigma K^*}^{(1)}, g_{N\Sigma K^*}^{(2)}$	-5.47, 0.0	SU(3) + ( $f_{N\Delta\rho} = 5.5$ )
$g_{\Xi\Sigma K^*}^{(1)}, g_{\Xi\Sigma K^*}^{(2)}$	-5.47, 0.0	SU(3) + ( $f_{N\Delta\rho} = 5.5$ )
$\kappa_{\Sigma^+\gamma}, \kappa_{\Sigma^0\gamma}, \kappa_{\Sigma^-\gamma}$	2.11, 0.32, -1.47	quark model [18]

TABLE III: Electromagnetic transition coupling constants employed in the present calculation. The last column cites the sources for the respective values. PDG refers to Ref. [2].

spin-1/2 $\leftrightarrow$ spin-1/2 transitions	$g_{BB'\gamma}$	
$\Lambda(1116) \leftrightarrow \Lambda(1405)$	0.99	quark model [19]
$\Lambda(1116) \leftrightarrow \Sigma(1193)$	1.61	PDG + quark model
$\Lambda(1405) \leftrightarrow \Sigma(1193)$	1.21	quark model [19]
spin-1/2 $\leftrightarrow$ spin-3/2 transitions	$(g_1, g_2)$	
$\Lambda(1116) \leftrightarrow \Lambda(1520)$	$(\pm 1.26, 0.0)$	CLAS data [20]
$\Lambda(1116) \leftrightarrow \Sigma^0(1385)$	$(2.81, -2.37)$	chiral quark model [21]
$\Sigma^0(1193) \leftrightarrow \Lambda(1520)$	$(\pm 2.22, 0.0)$	PDG based on SU(3) assumption
$\Sigma^+(1193) \leftrightarrow \Sigma^+(1385)$	$(2.68, -0.72)$	chiral quark model [21]
$\Sigma^0(1193) \leftrightarrow \Sigma^0(1385)$	$(0.40, 0.31)$	chiral quark model [21]
$\Sigma^-(1193) \leftrightarrow \Sigma^-(1385)$	$(1.15, -0.58)$	chiral quark model [21]
$\Xi^0(1530) \leftrightarrow \Xi^0(1318)$	$(3.02, -2.40)$	chiral quark model [21]
$\Xi^-(1530) \leftrightarrow \Xi^-(1318)$	$(0.56, -0.16)$	chiral quark model [21]
$g_{KK^*\gamma}^c$	0.41	PDG + SU(3)
$g_{KK^*\gamma}^0$	-0.63	PDG + SU(3)

for higher-mass resonances,  $\Lambda(1800)1/2^-$  and  $\Lambda(1890)3/2^+$ , as has been explained before.

### III. RESULTS

We now turn our attention to the results of the present model. The strategy we follow here is as follows. For a given choice of the ps-pv mixing parameter and the signs of the coupling constants mentioned in items a) and b) above, we adjust the parameters of the baryonic form factor mentioned in item c) to reproduce the preliminary total cross section data [9] in the  $\gamma p \rightarrow K^+ K^+ \Xi^-$  channel. We note that, in general, short-range processes are very sensitive to the hadronic off-shell form factors. In the present reaction, not only the absolute normalization, but also the energy dependence of the total cross section is found to be extremely sensitive to the baryonic form factor given in Eq. (A.20) for low-mass resonance contributions. We also mention that the coupling constants used in the present model calculation were taken as the centroid values of those quoted in PDG [2] and other hadron model predictions whenever available. Hence, since these coupling constants generally are subject to considerable uncertainties, large uncertainties of comparable size can be expected for the resulting fitted parameters of our model.

#### A. Low-mass resonances

We will first discuss the results considering only the low-mass hyperons [ $\Lambda(1116)$ ,  $\Lambda(1405)$ ,  $\Lambda(1520)$ ,  $\Sigma(1190)$ ,  $\Sigma(1385)$ ,  $\Xi(1318)$ , and  $\Xi(1530)$ ] whose relevant coupling constants can be determined from independent sources

as given in Tables II and III.<sup>5</sup> Here, the signs of the coupling constants mentioned in item b) in the previous Section are chosen to be all positive. The adjusted baryonic form-factor parameters are  $\Lambda_B = 1225$  MeV and  $n = 2$  for both the ps- ( $\lambda = 1$ ) and pv-coupling ( $\lambda = 0$ ) choices.<sup>6</sup> The resulting total cross sections are shown in Fig. 2 for both choices of the ps-pv mixing parameter  $\lambda = 0$  and  $\lambda = 1$ . The solid curves in Fig. 2 are the sum of all contributions and reproduce the basic features exhibited by the available preliminary data from the CLAS Collaboration [9] quite well. The predicted total cross sections for the other channels  $\gamma p \rightarrow K^+ K^0 \Xi^0$ ,  $\gamma n \rightarrow K^+ K^0 \Xi^-$ , and  $\gamma n \rightarrow K^0 K^0 \Xi^0$  are much larger than those for the  $\gamma p \rightarrow K^+ K^+ \Xi^-$  channel. Both choices of the ps-pv mixing parameter  $\lambda (= 0, 1)$  yield results (solid curves) which are close to each other in the energy region considered, especially, in the  $\gamma p \rightarrow K^+ K^+ \Xi^-$  channel where the data exist. However, their dynamical contents are quite different. The dashed curves correspond to the contributions from the diagrams in Fig. 1 which involve only the spin-1/2 hyperons in the intermediate state, while the dash-dotted curves correspond to those involving *one or more* spin-3/2 hyperons. One can see that the latter dominates in all the channels for the ps-coupling choice, while the former can be the dominant contribution for the pv-coupling choice depending on the reaction chan-

<sup>5</sup> We have also considered the  $\Delta(1232)$  resonance which may contribute to the present reaction through diagram (c) in Fig. 1. However, its contribution is negligibly small.

<sup>6</sup> We have varied the value of  $n$  together with the cutoff parameter  $\Lambda_B$ , and found that  $n = 2$  gives a good description of the preliminary total cross section data not only in the magnitude but in the energy dependence as well. For  $n = 1$ , the total cross section keeps increasing as the incident photon energy increases.

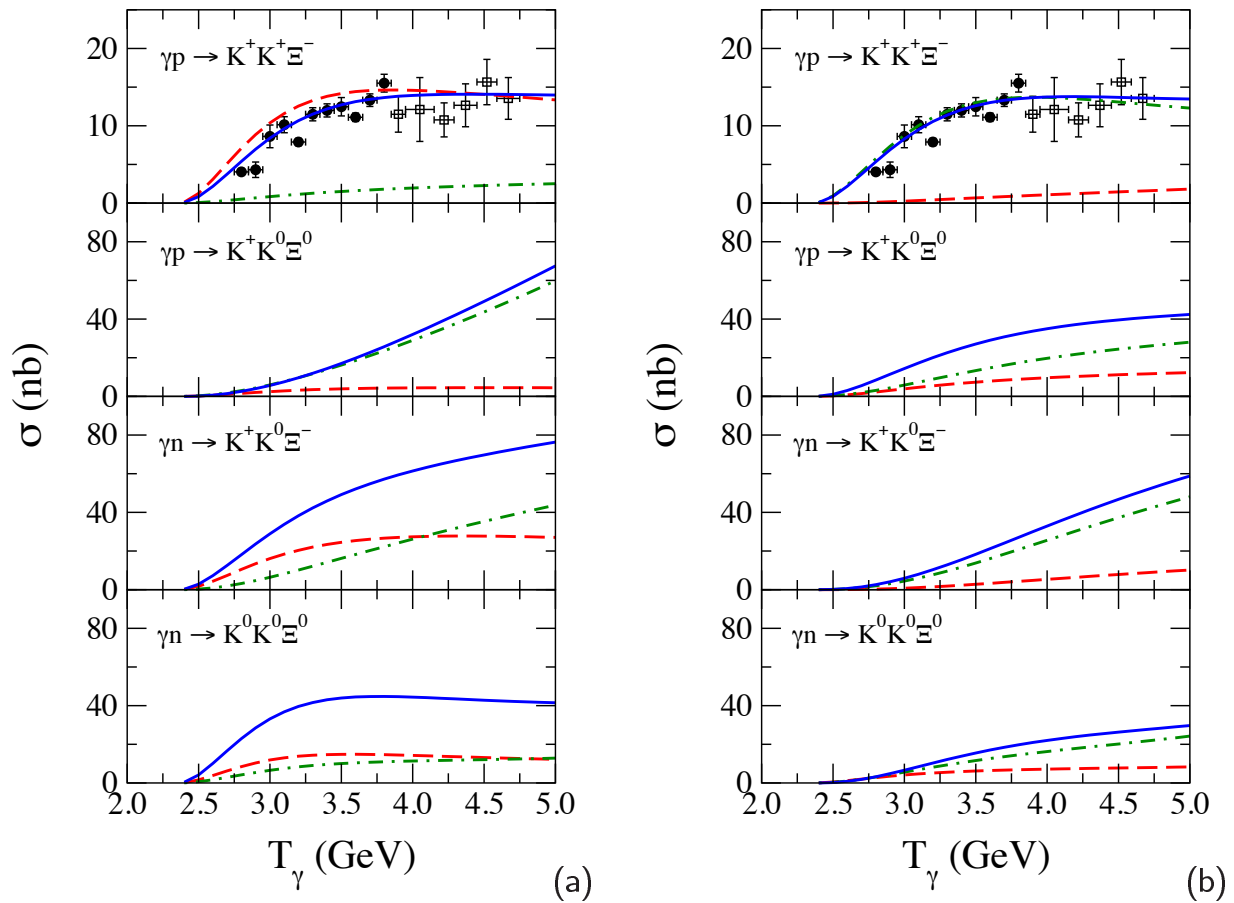


FIG. 2: (Color online) Total cross sections for  $\gamma N \rightarrow KK\Xi$  according to the mechanisms shown in Fig. 1 as a function of photon incident energy  $T_\gamma$  for (a) pseudovector ( $\lambda = 0$ ) and (b) pseudoscalar ( $\lambda = 1$ ) couplings. The dashed curves correspond to the contribution from the diagrams involving only the spin-1/2 hyperons, while the dash-dotted curves correspond to the contribution from the diagrams involving one or more spin-3/2 hyperons. The solid curves represent the total contribution. The (preliminary) data are from Ref. [9], where the open boxes are obtained without the differential cross section measurement.

nel. Note, especially, that in the  $\gamma p \rightarrow K^+ K^+ \Xi^-$  channel, the dominant contribution comes from the diagrams involving only spin-1/2 hyperons for the pv-coupling and from the diagrams involving one or more spin-3/2 hyperons in the case of the ps-coupling choice.

Shown in Fig. 3 is the dynamical content of our model for the pv-coupling choice. We see that among the spin-1/2 hyperon contributions [Fig. 3(a)] to the total cross section results in Fig. 2, the dominant one is by far the spin-1/2  $\leftrightarrow$  spin-1/2 radiative transition represented by the diagram Fig. 1(d) with  $Y \neq Y'$ . The other diagrams yield negligible contributions. Among the diagrams containing one or more spin-3/2 hyperon, the dominant contributions are either the spin-3/2  $\leftrightarrow$  spin-1/2 radiative transition or the spin-3/2 resonance contribution, Fig. 1(d) with  $Y = Y'$ , depending on the reaction channel.

Similarly, Fig. 4 shows the dynamical content of our model for the ps-coupling choice. Here only those diagrams involving one or more spin-3/2 hyperon are shown. The contributions from the spin-1/2 hyperons are small

in all the reaction channels as shown in Fig. 2. As one can see, in the  $\gamma p \rightarrow K^+ K^+ \Xi^-$  and  $\gamma n \rightarrow K^0 K^0 \Xi^0$  channels, the spin-3/2  $\leftrightarrow$  spin-1/2 radiative transitions (solid curves) are, by far, the dominant processes. In other channels, there are competing mechanisms, namely, the spin-3/2 resonance contribution represented by Fig. 1(d) with  $Y = Y'$  (dashed curves) and the  $\Xi(1530) \leftrightarrow \Xi(1318)$  radiative transition, Fig. 1(e) (dash-dotted curves), in addition to the spin-3/2  $\leftrightarrow$  spin-1/2 radiative transitions.

Figure 5 shows the model predictions for the angular distributions of the produced cascade  $\Xi^-$  and kaon  $K^+$  in the center-of-mass frame of the total system. They correspond to the total cross section results of Fig. 2. We present the results for four different photon energies, spanning the energy region relevant to ongoing cascade photoproduction experiment at JLab [9, 22]. One can see that the cascade angular distribution becomes forward-angle peaked as the energy increases, while the  $K^+$  distribution becomes backward-angle peaked. This tendency is stronger with the ps-coupling choice. Here, we note that the shapes of the angular distributions are sensitive to

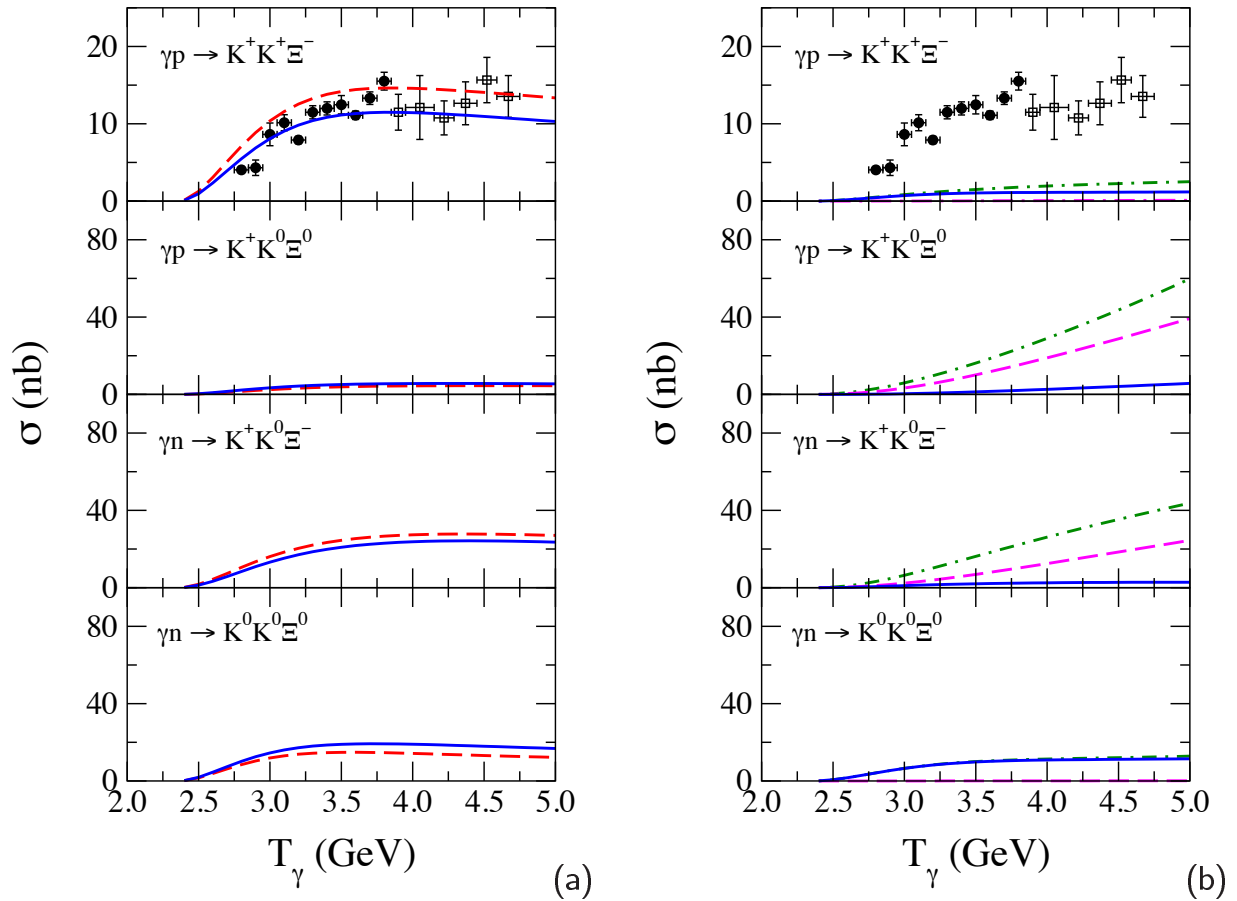


FIG. 3: (Color online) (a) Breakdown of the spin-1/2 hyperon contributions to the total cross section for  $\gamma N \rightarrow KK\Xi$  shown in Fig. 2(a) for the pv-coupling choice according to the mechanisms shown in Fig. 1. The solid curves correspond to the contributions from the radiative transition diagram Fig. 1(d) with  $Y \neq Y'$  and the dashed curves to the total contribution from the spin-1/2 hyperons [same as the dashed curves in Fig. 2(a)]. (b) Same as (a) but for the processes involving one or more spin-3/2 hyperon. The dashed curves correspond to the spin-3/2 resonance contribution Fig. 1(d) with  $Y = Y'$  and the dash-dotted curves to the total contribution [same as the dash-dotted curves in Fig. 2(a)]. The solid curves correspond to the spin-3/2  $\leftrightarrow$  spin-1/2 radiative transition diagram Fig. 1(d) with  $Y \neq Y'$ . Contributions from the other diagrams in Fig. 1 are too small and, therefore, not shown here. The (preliminary) data are from Ref. [9].

the production mechanism. In particular, the exhibited shapes of the angular distributions are due to the dominance of the spin-1/2  $\leftrightarrow$  spin-1/2 hyperon radiative transitions [diagram Fig. 1(d)] for the pv-coupling choice and of the spin-3/2  $\leftrightarrow$  spin-1/2 hyperon radiative transitions for the ps-coupling choice, as shown by the corresponding dotted lines in the left panel of Fig. 5 for  $T_\gamma = 3.80$  GeV. Note that the different behavior of the angular distribution in the forward (backward)  $\Xi^-$  ( $K^+$ ) angles between the pv- and ps-coupling choices is caused by the radiative transition diagrams. We also note that the  $\Xi^-$  and  $K^+$  angular distributions are not completely independent of each other, because, in the center-of-momentum (c.m.) frame of the system, energy-momentum conservation demands that if one of the  $K^+$  is emitted in forward (backward) angles, the  $\Xi^-$  be emitted necessarily in backward (forward) angles for sufficiently high incident energies. We emphasize that the shape of the angular distribution

can change completely from that predicted in Fig. 5 if the dominant production mechanism is the  $t$ -channel  $K$ -exchange current [diagrams Figs. 1(a,b)] instead of the radiative transition current.<sup>7</sup> As we shall show in the following subsection, such a situation is possible when contributions from the higher mass resonances are considered.

Displayed in Fig. 6 are the predictions for the  $K^+\Xi^-$  and  $K^+K^+$  invariant-mass distributions, respectively, in  $\gamma p \rightarrow K^+K^+\Xi^-$ . Again, they correspond to the total cross-section results in Fig. 2. As has been pointed out already in connection with the total cross sections in Fig. 2, here the results do not exhibit any resonance structure

<sup>7</sup> Among the various production mechanisms considered in this work, only the  $t$ -channel  $K$ -exchange process [diagram Fig. 1(a)] exhibits the backward-peaked angular distribution for  $\Xi^-$ .

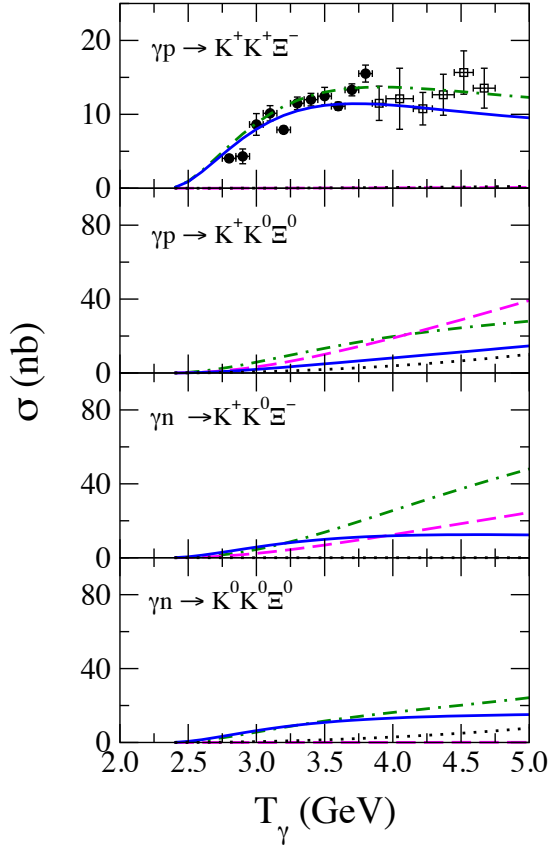


FIG. 4: (Color online) Same as Fig. 3(b) but with the ps-coupling choice. The solid curves correspond to the contribution from the radiative transition diagram Fig. 1(d) with  $Y \neq Y'$  and the dashed curves to the spin-3/2 resonance contribution Fig. 1(d) with  $Y = Y'$ . The dotted curves represent the  $\Xi(1530) \leftrightarrow \Xi(1318)$  radiative transition of Fig. 1(e). The dash-dotted curves are the total spin-3/2 contributions as shown in Fig. 2(b). The other diagrams of Fig. 1 yield too small contributions and are not shown.

in the  $K^+\Xi^-$  invariant mass distribution because all the hyperon resonances considered here lie below the production threshold. The absence of any structure in the  $K^+K^+$  invariant mass distribution is due to the absence of  $S = +2$  exotic meson production.

### B. Higher-mass resonances (I)

We now explore the possible influence of the higher-mass  $S = -1$  hyperon resonances. Since the higher hyperon resonances lie close to or above the threshold energy of  $\Xi$  production (see Table I), it is natural to expect them to play a more prominent role than the low-mass hyperons. However, because of the lack of sufficient information to extract the necessary parameter values associated with these high-mass resonances, here we consider the hyperon resonances  $\Lambda(1800)1/2^-$  and  $\Lambda(1890)3/2^+$ , as discussed in Sec. II. Since no parameters other than the

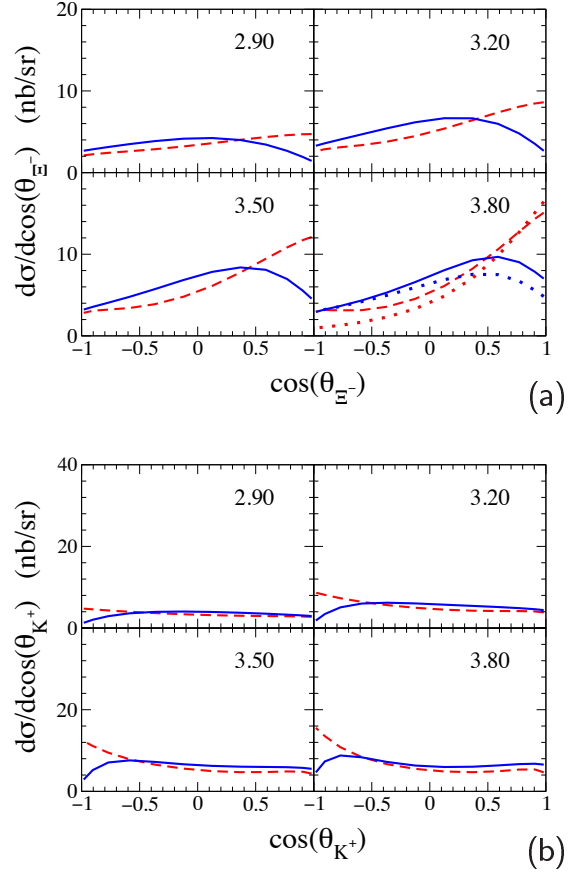


FIG. 5: (Color online) Predicted angular distributions for the (a)  $\Xi^-$  and (b)  $K^+$  particles for  $\gamma p \rightarrow K^+ K^+ \Xi^-$  in the center-of-mass frame corresponding to the results of Fig. 2 with the pv- (solid curves) and ps-coupling (dashed curves) choices. The number in the right upper corner of each figure indicates the incident photon energy  $T_\gamma$  in units of GeV. The dotted curves at  $T_\gamma = 3.80$  GeV in (a) represent the radiative transition contributions corresponding to Fig. 1(d) with  $Y \neq Y'$ .

$NYK$  coupling constants  $g_{NYK}$  are known, we consider the diagrams of Figs. 1(a)–(g), where  $Y = Y'$  in diagram Fig. 1(d). This introduces the coupling constant  $g_{\Xi Y K}$  as the additional free parameter as we neglect the magnetic moments of these  $\Lambda$  resonances. Then, since only the product  $g_{NYK}g_{\Xi Y K}$  enters into the calculation of these processes, we explore the influence of the higher-mass resonances as a function of this product of the coupling constants.

Figure 7 shows the results for the total cross sections for  $\gamma N \rightarrow K K \Xi$  when the above-mentioned higher-mass resonances are included in addition to the low-mass resonances discussed in the previous subsection. Here, the product of the coupling constants is fixed to be  $g_{N\Lambda K}g_{\Xi\Lambda K} = 2$  for both resonances assuming that  $g_{\Xi\Lambda K}$  has the same order of magnitude as  $g_{N\Lambda K}$ . The values of  $\Lambda_B = 1170$  MeV and  $n = 2$  were readjusted to reproduce the measured total cross section [9]. Everything else is kept the same as in the previous subsection. We



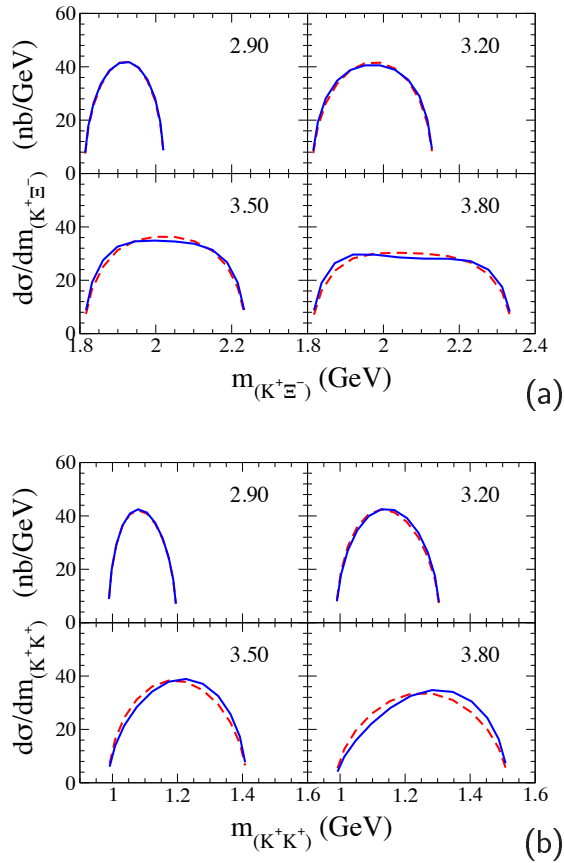


FIG. 6: (Color online) Predicted invariant-mass distributions for (a)  $K^+\Xi^-$  and (b)  $K^+K^+$  for  $\gamma p \rightarrow K^+K^+\Xi^-$  corresponding to the results of Fig. 2 with the pv- (solid curves) and ps-coupling (dashed curves) choices. The number in the right upper corner of each subpanel indicates the incident photon energy in units of GeV.

then obtain essentially the same results as in the previous section where only the low-mass hyperons were considered. This shows that the total cross sections alone are unable to distinguish the contributions from the low- and high-mass hyperons. We emphasize, however, that this is not the case when we consider the total cross section in conjunction with the angular distributions of the produced cascade and/or kaons. In fact, for example, when we insist that the resulting shape of the  $\Xi^-$  and/or  $K^+$  angular distributions be of the form shown in Fig. 9 (see below), we could not reproduce the measured energy dependence of the total cross section in  $\gamma p \rightarrow K^+K^+\Xi^-$  without both the high-mass hyperons considered here. This reveals that this reaction is, in fact, suited for extracting information on the high-mass hyperons. We also repeat that the  $t$ -channel  $\bar{K}N \rightarrow K\Xi$  process and meson-production processes are absent in the present reaction, which is a feature that makes this reaction more suitable for studying high-mass hyperon resonances.

The dynamical content of the model considered in this subsection is shown in Fig. 8 for the case of the pv-coupling choice. As can be seen, contrary to the re-

sults of the previous subsection, we now have the  $t$ -channel  $K$ -exchange mechanism [Figs. 1(a,b)] competing with the radiative transition mechanism depending on the reaction channels. Similar observations can be made for the case of the ps-coupling choice. Note that in the  $\gamma p \rightarrow K^+K^+\Xi^-$  channel, the  $K$ -exchange is, by far, the dominant contribution arising from the diagrams involving the spin-3/2 hyperons. Of course, in the  $\gamma n \rightarrow K^0K^0\Xi^0$  channel, the  $K$ -exchange mechanism is simply absent.

In Fig. 9, we show the model predictions for the angular distributions of the produced  $\Xi^-$  and  $K^+$  in the c.m. frame of the total system. They correspond to the total cross section results of Fig. 7. Here we see that the shape of the angular distributions are just the opposite to those shown in Fig. 5, where only the low-mass hyperons were considered. Here, the backward- (forward-) peaked angular distribution of  $\Xi^-$  ( $K^+$ ) is due to the dominance of the  $t$ -channel  $K$ -exchange process, Figs. 1(a,b). This is illustrated in Fig. 10 at  $T_\gamma = 3.80$  GeV for the pv- and ps-coupling choices. It is a simple matter of kinematics that the  $t$ -channel processes contribute mostly for low  $t$  and high incident energies which leads to the forward-peaked  $K^+$  angular distribution as the incident photon energy increases. In the c.m. frame this, in turn, leads to the backward-peaked  $\Xi^-$  angular distribution. It is obvious, then, that the angular distributions can tell us about the  $\Xi^-$  production mechanism, in particular, whether the dominant mechanism is the radiative transitions (as in the previous subsection) or the  $t$ -channel  $K$ -exchange (as shown here). In the  $\gamma n \rightarrow K^0K^0\Xi^0$  reaction channel, the latter mechanism, of course, is absent.

In Fig. 11, we display the predictions for the  $K^+\Xi^-$  and  $K^+K^+$  invariant-mass distributions in  $\gamma p \rightarrow K^+K^+\Xi^-$ . Again, they correspond to the total cross section results in Fig. 7. Since we do not have  $S = +2$  exotic meson production, the  $K^+K^+$  invariant-mass distributions are very similar to those shown in Fig. 6 and have no structure. However, the  $K^+\Xi^-$  invariant-mass distributions are quite different from those shown in Fig. 6 for, here, they exhibit two bump structures as the incident photon energy increases. The  $\Lambda(1800)$  hyperon is just below the threshold and contributes to the sharp rise of the  $K^+\Xi^-$  invariant-mass distribution near the threshold. The bump at lower invariant mass is due to the  $\Lambda(1890)$  hyperon. The second bump at higher invariant mass is due to the same hyperon  $\Lambda(1890)$ , but comes from the diagram Fig. 1(b). We emphasize that the appearance of a second bump at a higher invariant mass is a general feature of two-meson production reactions and should not be confused with the existence of another resonance with a higher mass. Note that the position of the second bump changes depending on the photon energy, which evidently makes it clear that the structure does not come from a resonance.

As we have shown, the angular distributions of  $\Xi^-$  and  $K^+$  are sensitive to the production mechanism of  $\gamma p \rightarrow K^+K^+\Xi^-$ . In particular, depending on whether

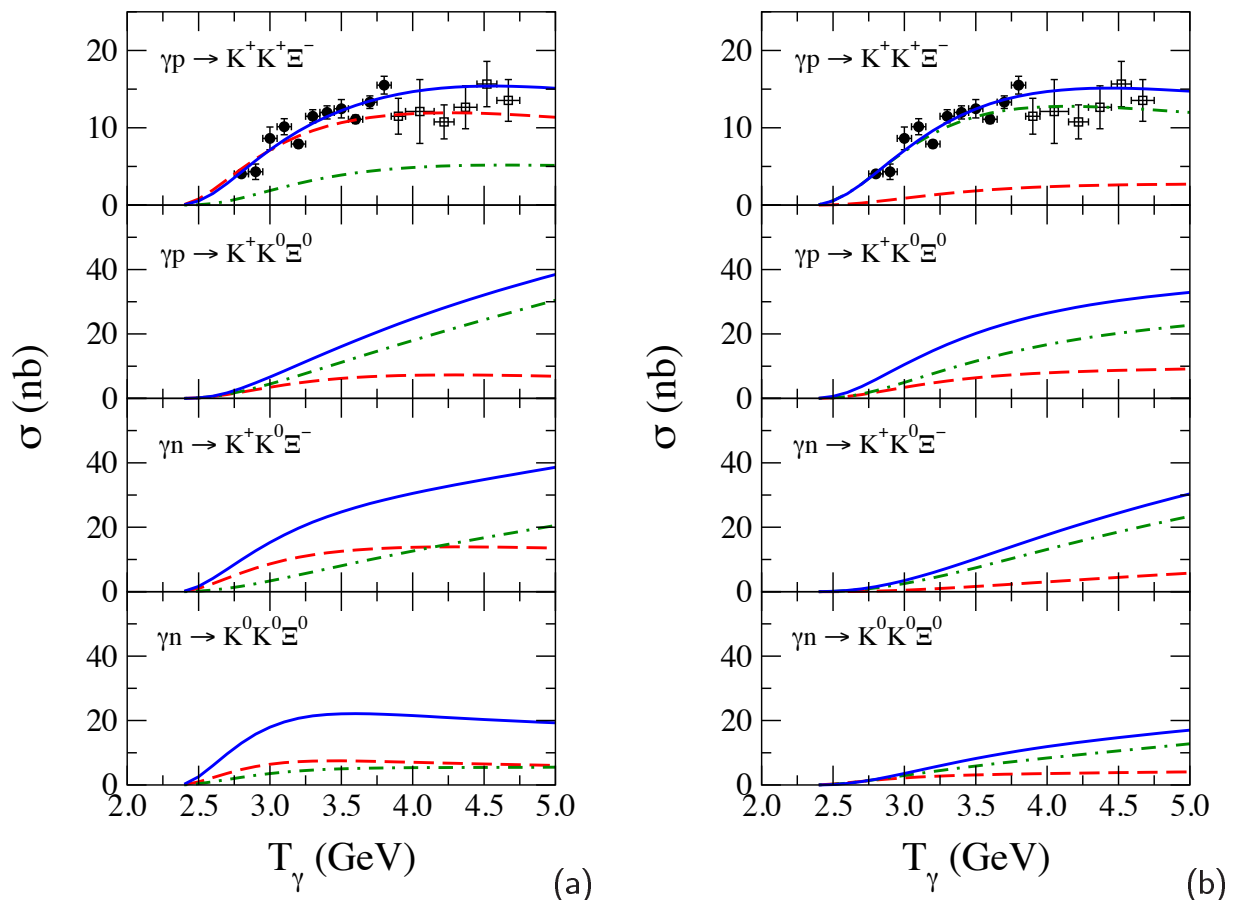


FIG. 7: (Color online) Same as Fig. 2, but with the addition of the higher-mass hyperons  $\Lambda(1800)1/2^-$  and  $\Lambda(1890)3/2^+$ .

the dominant mechanism is the radiative transition or  $t$ -channel  $K$ -exchange, the shape of the angular distribution can change completely. However, one should keep in mind that most of the parameters in the present work have been fixed based on quark models and/or SU(3) symmetry considerations in combination with independent experimental information whenever available. The parameter values estimated in this way may, therefore, be subject to considerable uncertainties. In particular, one cannot completely discard the possibility that reaction mechanisms other than the  $t$ -channel  $K$ -exchange might lead, for example, to backward- (forward-) peaked  $\Xi^-$  ( $K^+$ ) angular distribution through the interference with the radiative transition mechanisms. It is interesting, therefore, to look for an independent observable which is also sensitive to the production mechanisms other than the differential cross sections.

Our predictions for the photon beam asymmetry,

$$\Sigma_B \equiv \frac{\sigma(\lambda = +1) - \sigma(\lambda = -1)}{\sigma(\lambda = +1) + \sigma(\lambda = -1)}, \quad (3)$$

where  $\sigma(\lambda)$  denotes the cross section with the linear photon polarization along the  $y$ -axis ( $\lambda = +1$ ) and  $x$ -axis ( $\lambda = -1$ ), are shown in Fig. 12 as a function of the  $\Xi^-$  emission angle. The solid and dashed curves cor-

respond to the predictions of the model in the present work with the pv- and ps-coupling choices, respectively. In Fig. 12(b), we display the results of the model of the present subsection. First, we see that both curves are practically the same. Second, they are largely negative at backward angles, a feature that becomes more pronounced as the photon energy increases. This is a characteristic feature of the  $t$ -channel  $K$ -exchange mechanism. As noted before,  $t$ -channel processes contribute mostly at small  $t$  and higher incident energies. In the c.m. frame, this implies a backward-angle emission of the  $\Xi^-$  hyperon. Now, the beam asymmetry due to the  $t$ -channel  $K$ -exchange corresponding to Fig. 1(a) alone is identical to  $\Sigma_B = -1$ , since the three-momentum  $\mathbf{q}_1$  of the emitted  $K^+$  can be chosen to be in the  $xz$ -plane without loss of generality. Given in Fig. 12(a) are the corresponding predictions of the model discussed in the previous subsection, Sec. III A, where the radiative transition diagram [Fig. 1(d) with  $Y \neq Y'$ ] dominates. We see that they are small and positive for most  $\Xi^-$  emission angles, which is very different from the model results of the present subsection [Fig. 12(b)]. This, therefore, demonstrates that the beam asymmetry can be used as another independent observable to identify the relevant production mechanisms, i.e., whether the  $t$ -channel  $K$  exchanges

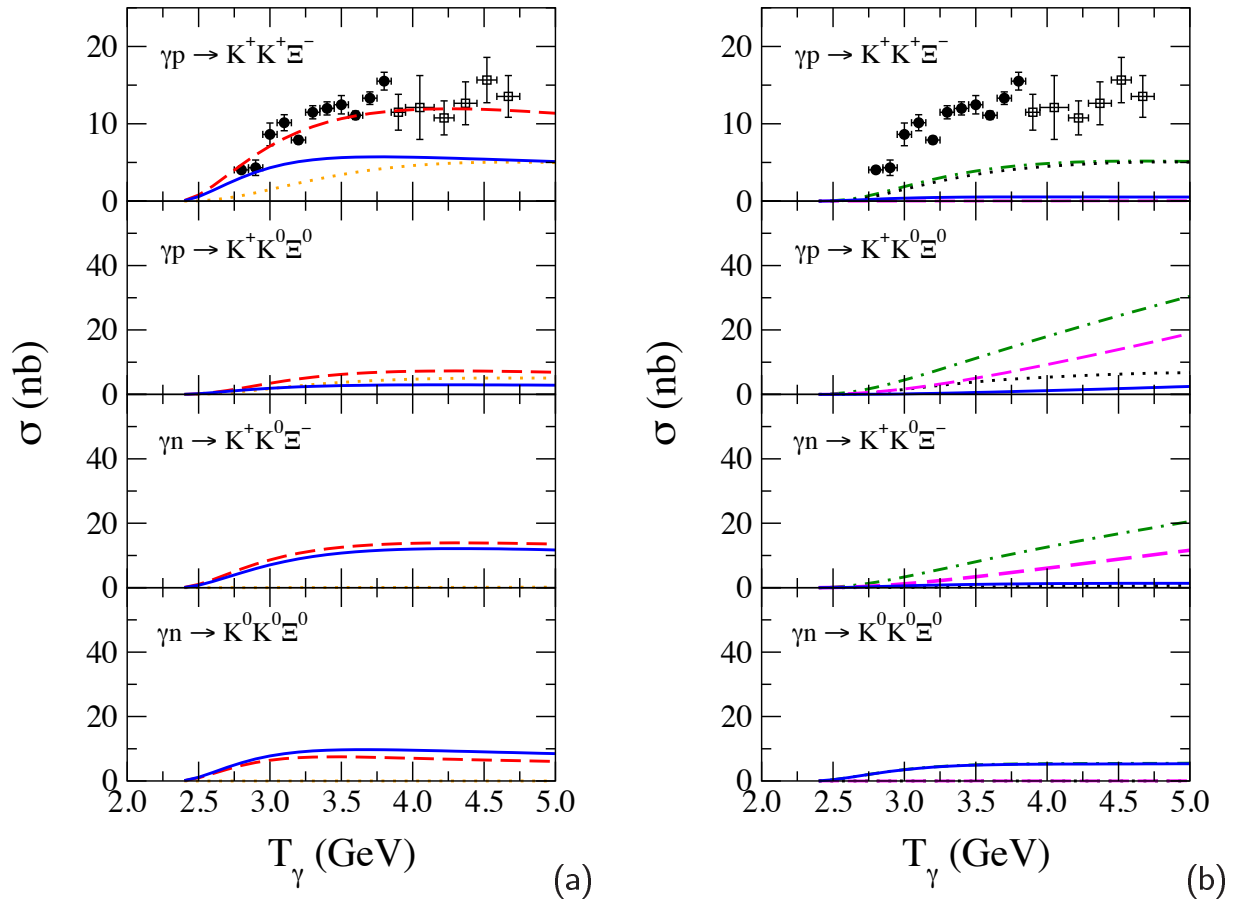


FIG. 8: (Color online) Same as Fig. 3, but for the results shown in Fig. 7(a) with the pv-coupling choice. (a) The solid curves correspond to the contribution from the radiative-transition diagram Fig. 1(d) with  $Y \neq Y'$  and the dotted curves to the  $K$ -exchange diagrams of Figs. 1(a,b). The dashed curves represent the total contributions from the spin-1/2 hyperons and are taken over from Fig. 7. (b) The dashed curves correspond to the diagram Fig. 1(d) with  $Y = Y'$  and the dotted curves to the  $K$ -exchange diagrams of Figs. 1(a,b). The solid curves are for the spin-3/2  $\leftrightarrow$  spin-1/2 radiative transition diagram Fig. 1(d) with  $Y \neq Y'$ . The dash-dotted curves are the total contribution taken over from Fig. 7(a). The other contributions are too small and are not shown here.

dominate or the radiative transition diagrams dominate.

Here, it should be noted that, in general, spin observables are much more sensitive to the details of theoretical models, in particular, to the background FSI effects. As mentioned in Sec. I, the latter is not considered in the present work. However, to the extent that the kaons couple strongly to the (high-mass) spin-1/2 hyperon resonances, the features just discussed above for the beam asymmetry should hold.<sup>8</sup> The same observation applies for the target asymmetry discussed below. For all the observables considered so far in the present work, the pv- and ps-coupling schemes give very similar results to each other, although the dynamical contents can differ substantially from each other. In particular, the dominant contribution to the total cross sections can arise

either from the spin-1/2 or spin-3/2 hyperons depending on the choice of the pv- or ps-coupling at the  $BYK$  vertex for spin-1/2 baryon  $B$  and hyperon  $Y$  (cf. Figs. 2 and 7). In an effort to distinguish between the two coupling schemes, we have computed the target asymmetry which is defined as

$$\Sigma_T \equiv \frac{\sigma(\lambda_N = +1) - \sigma(\lambda_N = -1)}{\sigma(\lambda_N = +1) + \sigma(\lambda_N = -1)}, \quad (4)$$

and found that it can provide a tool for testing these coupling schemes. Here,  $\sigma(\lambda_N = \pm 1)$  denotes the cross section with the polarized target nucleon along the  $\pm y$ -axis. In Fig. 13, the predictions of this subsection's model for the target asymmetry are shown. As can be seen, the predictions corresponding to the pv-coupling (solid curves) differ markedly from those corresponding to the ps-coupling (dashed curves) at backward angles. Note that the sensitivity to the ps-pv mixing parameter at backward angles is due to the strong  $t$ -channel  $K$ -exchange contribution and arises from the fact that

<sup>8</sup> Note that the pole part of the FSI is accounted for by the resonances.

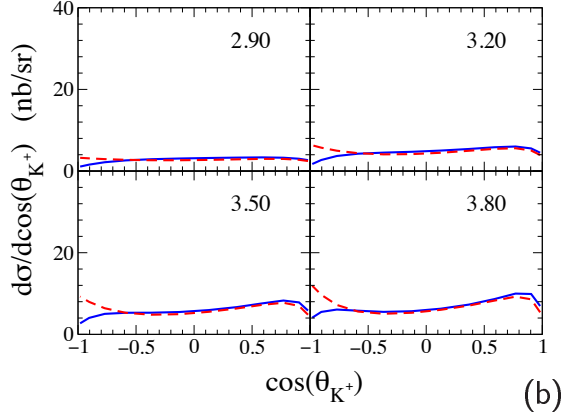
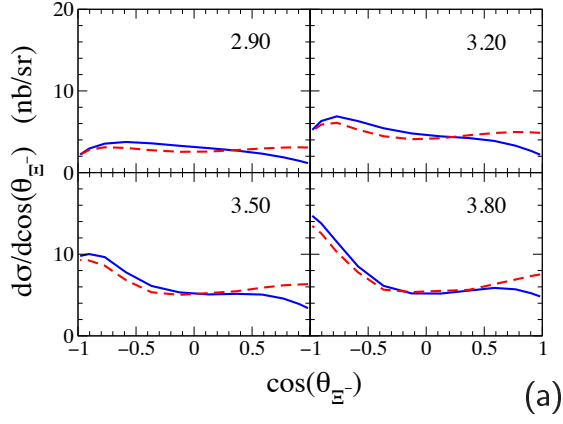


FIG. 9: (Color online) Same as Fig. 5, but for the results of Fig. 7.

the ps-coupling involves  $\gamma_5$  while the pv-coupling involves  $\gamma_5 q_\mu \gamma^\mu$  at the meson-baryon vertex. The latter leads to an amplitude which contains an extra  $\boldsymbol{\sigma} \cdot \mathbf{q}$  factor as compared to the former choice. Therefore, the target

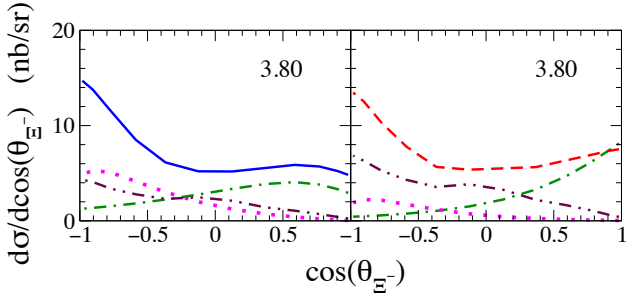


FIG. 10: (Color online) Same as Fig. 9 at  $T_\gamma = 3.80$  GeV. In the left panel, the dotted and dash-dotted curves correspond to the contributions from the  $t$ -channel  $K$ -exchange and radiative transition processes, respectively, [Figs. 1(a,b,d) with  $Y \neq Y'$ ] involving only the spin-1/2 hyperons. The dash-double-dotted curve is due to the  $t$ -channel  $K$ -exchange involving one or more spin-3/2 hyperons. They all correspond to the pv-coupling choice. Same in the right panel, but with the ps-coupling choice.

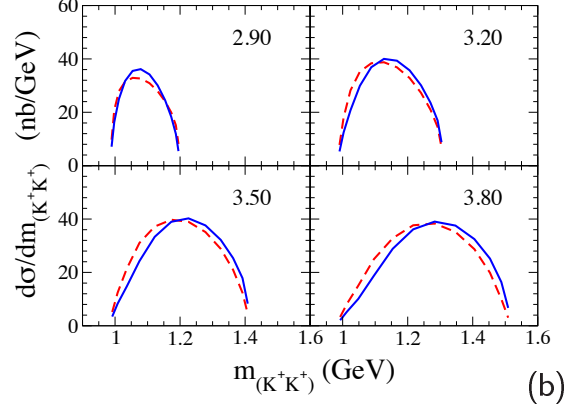
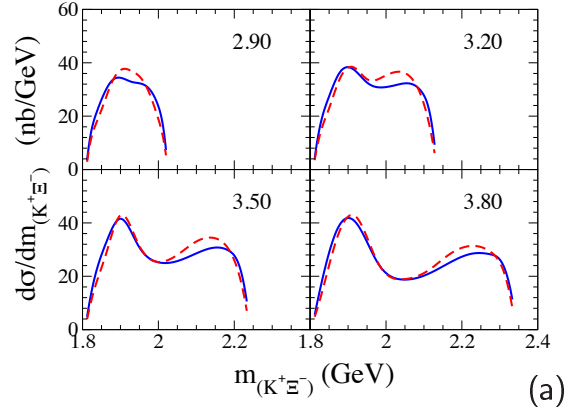


FIG. 11: (Color online) Same as Fig. 6, but for the results of Fig. 7.

asymmetry offers a potential means of distinguishing the two types of couplings at the  $BYK$  vertex. The larger difference between the pv- and ps-coupling at low energies arises from the  $\Lambda(1800)1/2^-$  resonance contribution which is just below the threshold energy.

### C. Higher-mass resonances (II)

In the remaining part of this Section we further explore the influence of the undetermined parameters in the present work. Specifically, in this subsection we consider the negative signs for the parameters mentioned in item b) of Sec. II. In this discussion, we restrict ourselves to the pv-coupling choice.

Presented in Fig. 14 are the results for the total cross sections. The cutoff parameter  $\Lambda_B = 1250$  MeV and the exponent  $n \rightarrow \infty$  have been readjusted to reproduce the preliminary total cross section data in the  $\gamma p \rightarrow K^+ K^+ \Xi^-$  reaction channel. The baryonic form factor in Eq. (A.20) then corresponds to a Gaussian form with the width of 1250 MeV. In addition, we have also adjusted slightly the mass of the two higher-mass hyperons to be  $m_{\Lambda 1/2^-} = 1850$  and  $m_{\Lambda 3/2^+} = 1950$  MeV to reproduce the total cross section data. Note that the PDG

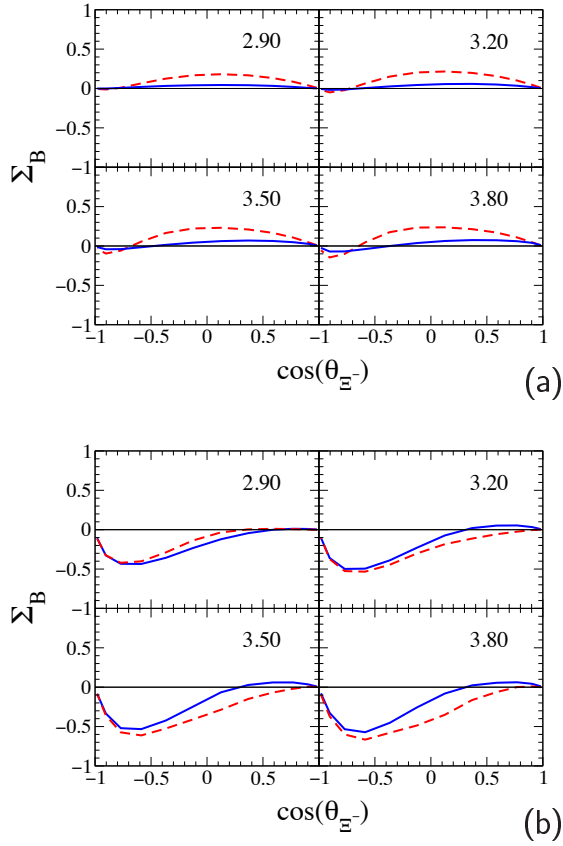


FIG. 12: (Color online) Photon asymmetry as a function of the  $\Xi^-$  emission angle in the c.m. frame in  $\gamma p \rightarrow K^+ K^+ \Xi^-$  for the models discussed in (a) Sec. III A (with only low-mass hyperons) and (b) Sec. III B [with, in addition, the higher-mass  $\Lambda(1800)$  and  $\Lambda(1890)$  hyperons], respectively. The solid and dashed curves correspond to the predictions of the model with the pv- and ps-coupling choices, respectively.

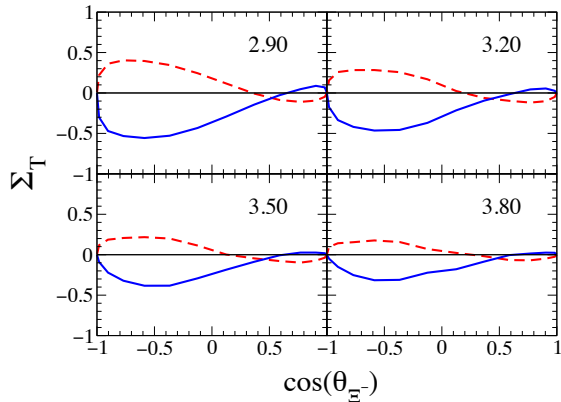


FIG. 13: (Color online) Target asymmetry as a function of the  $\Xi^-$  emission angle in the c.m. frame in  $\gamma p \rightarrow K^+ K^+ \Xi^-$ . The solid and dashed curves correspond to the predictions of the model in Sec. III B for the pv- and ps-coupling choices, respectively.

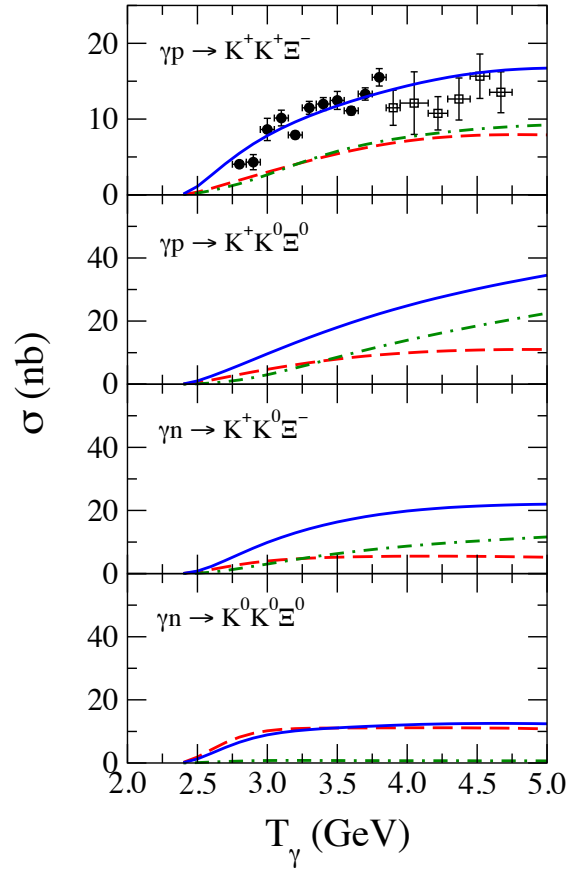


FIG. 14: (Color online) Same as Fig. 7(a), but with the signs of the coupling constants mentioned in item b) of Sec. II chosen to be negative.

masses for the  $\Lambda(1800)$  and  $\Lambda(1890)$  are in the range of 1720 ~ 1850 MeV and 1850 ~ 1910 MeV, respectively. The product of the coupling constants  $g_{N\Lambda K}g_{\Xi\Lambda K} = 2$  for both the  $\Lambda(1850)1/2^-$  and  $\Lambda(1950)3/2^+$  hyperons have been kept as in the previous subsection so as to result in the similar  $\Xi^-$  and  $K^+$  angular distributions as in Fig. 9. The corresponding angular distributions are displayed in Fig. 15.

Figure 16 presents the predictions for the  $K^+\Xi^-$  and  $K^+K^+$  invariant mass distributions, respectively, in  $\gamma p \rightarrow K^+K^+\Xi^-$ . They correspond to the total cross section results in Fig. 14 and exhibit similar features to those shown in Fig. 11 in the previous subsection, although here the two bumps are more symmetric.

#### D. Higher-mass resonances above 2 GeV

The structure of the  $K^+\Xi^-$  invariant mass distribution predicted in Figs. 11 and 16 may change qualitatively if there is a significant contribution from some additional resonances in the 2.0 GeV mass region. In fact, there are well established spin-5/2 and -7/2  $\Lambda$  and  $\Sigma$  hyperons with masses around 2.05 GeV (cf. Table I) which may poten-

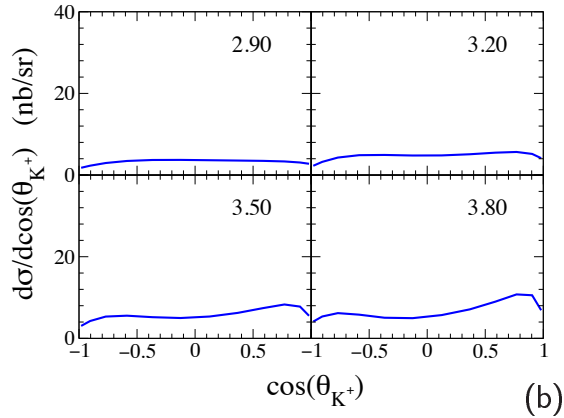
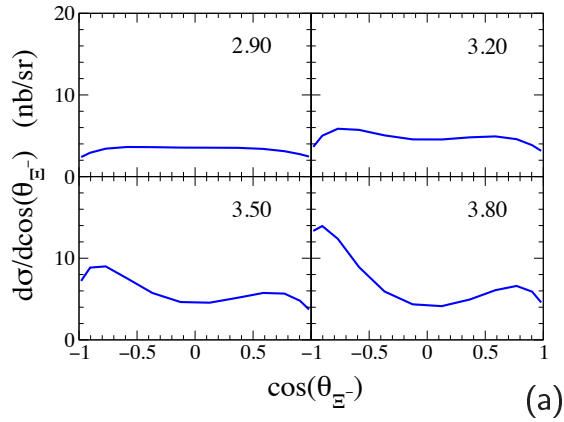


FIG. 15: (Color online) Same as Fig. 9, but for the results of Fig. 14.

tially affect the  $K^+\Xi^-$  invariant mass distribution in this energy region. It is conceivable, therefore, that these resonances may be capable to fill up the valley between the two bumps in the predicted invariant mass distribution seen on the left-hand sides of Figs. 11 and 16. However, as explained in the Introduction, since there is no detailed dynamical information available about these resonances, their inclusion into our model would be very speculative and an investigation of the detailed effects of such higher-spin resonances should be left for future work. However, the question as to whether some resonance in the 2-GeV region can fill the valley can be addressed qualitatively by simulating high-spin resonances by a *fictitious* hyperon resonance in this energy region. Concretely, therefore, in addition to the known  $\Lambda(1800)1/2^-$  and  $\Lambda(1890)3/2^+$  states (and the low-mass hyperons considered in the previous subsections), we employ a (fictitious)  $\Lambda(2050)3/2^+$  resonance with  $\Gamma_{\Lambda(2050)} = 200$  MeV. The product of the coupling constants  $g_{N\Lambda K}g_{\Xi\Lambda K} = 2$  for  $\Lambda(1800)$ ,  $g_{N\Lambda K}g_{\Xi\Lambda K} = 1.2$  for  $\Lambda(1890)$ , and  $g_{N\Lambda K}g_{\Xi\Lambda K} = (1.2)^2$  for  $\Lambda(2050)$  are used, in conjunction with the cutoff parameter  $\Lambda_B = 1250$  MeV and  $n \rightarrow \infty$  in order to reproduce the measured total cross section [9] and keep the shape of the  $\Xi^-$  and  $K^+$  angular distributions backward- and forward-peaked, respectively, as in Fig. 15. We re-

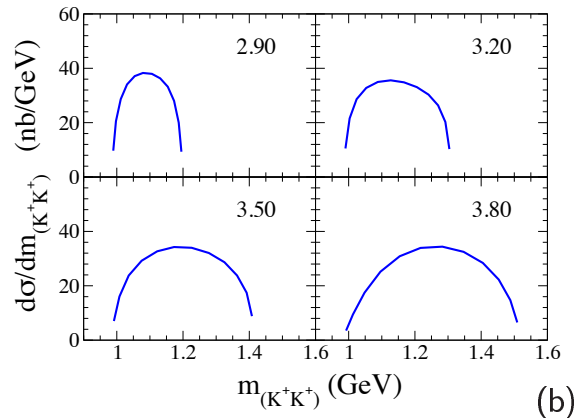
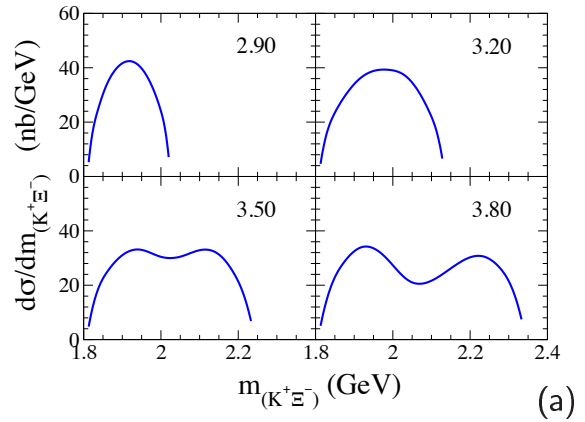


FIG. 16: (Color online) Same as Fig. 6, but for the results of Fig. 14.

frain from showing the corresponding total cross section and angular distribution results here because they are practically the same as those shown in Figs. 14 and 15.

As can be seen in Fig. 17, the bump structures indeed have disappeared completely due to the  $\Lambda(2050)$  reso-

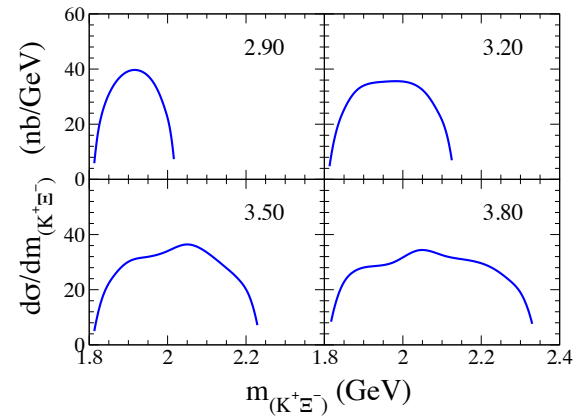


FIG. 17: (Color online) Same as Fig. 16, but with the additional (fictitious)  $\Lambda(2050)3/2^+$  resonance (see text for detailed explanation).

nance whose contribution fills up the valley in the  $K^+\Xi^-$  invariant mass around  $m_{K^+\Xi^-} = 2$  GeV seen in Figs. 11 and 16. We may expect, therefore, that a similar effect will also occur when the known higher-spin resonances in this energy range are considered.

These considerations show that the study of  $\Xi$  photoproduction may provide useful information about higher-mass hyperon resonances which makes it all the more desirable to have more rigorous investigations that provide a better understanding of the dynamics of such higher-mass and higher-spin resonances.

#### IV. SUMMARY

In summary, we have explored the reaction  $\gamma N \rightarrow KK\Xi$  within a relativistic meson-exchange model of hadronic interactions. This is the first theoretical investigation of this reaction in connection with the cascade spectroscopy program initiated recently by the CLAS Collaboration at JLab [5–7, 9].

Most of the parameters of the model involving the low-mass hyperons in the intermediate states were determined from the empirical data and/or quark models and SU(3) symmetry considerations. It is found that the dominant reaction mechanism arising from those low-mass hyperons is the radiative transitions [cf. Fig. 1(d) with  $Y \neq Y'$ ], especially, for producing the  $\Xi^-$  in the  $\gamma p \rightarrow K^+K^+\Xi^-$  reaction, which is currently under investigation by the CLAS Collaboration at JLab [9]. This production mechanism is also found to lead to a forward- (backward-) peaked angular distribution of the produced  $\Xi^-$  ( $K^+$ ).

We have also explored the possible influence of the higher-mass hyperons in  $\gamma N \rightarrow KK\Xi$ , which are expected to contribute more significantly to this reaction than the low-mass hyperons because they are energetically more favored than the latter resonances. The difficulty in quantifying the contributions from these high-mass hyperons is the complete lack of information about the strengths of their couplings to the cascade baryons. Nevertheless, we have shown that these high-mass resonances may lead to a dominance of the  $t$ -channel  $K$ -exchange mechanism for producing the cascade baryons. Moreover, the angular distribution of the produced  $\Xi^-$  and the photon asymmetry in  $\gamma p \rightarrow K^+K^+\Xi^-$  were shown to offer two independent ways of possibly distinguishing between the  $t$ -channel  $K$ -exchange and the radiative transitions as the dominant mechanisms for  $\Xi^-$  photoproduction. The target asymmetry was also shown to possibly impose constraints on the ps-pv mixing parameter at the  $BYK$  vertex involving spin-1/2 baryons.

In addition, the  $K^+\Xi^-$  invariant-mass distribution in  $\gamma p \rightarrow K^+K^+\Xi^-$  yields a clear information on the high-mass hyperon resonance contributions. However, care must be taken to avoid misidentifying the second bump structure, which is kinematic in origin, with the formation of a higher-mass resonance during the reaction.

Moreover, the non-existence of the bump structure in the  $K^+\Xi^-$  invariant mass distribution may happen due to the overlap of broad resonances as we have explicitly shown in Fig. 17. These findings show that  $\Xi$  photoproduction is indeed well suited for investigating the properties of higher-mass hyperon resonances.

We conclude from the present work that one needs to consider concomitantly not only the total cross sections and their angular distributions but also other observables, such as invariant-mass distributions, beam asymmetries, and target asymmetries, in order to learn about the cascade photoproduction reaction. This is required, especially when the reaction mechanism is unclear as in the current case. These observables have different role in identifying the production mechanisms.

Finally, the present effort is just a first step toward building a more complete and realistic model for describing cascade baryon photoproduction off nucleons. Our findings should be useful for future investigation of this reaction both experimentally and theoretically. Experimentally, we are aware of that the CLAS Collaboration is currently analyzing the  $\gamma p \rightarrow K^+K^+\Xi^-$  reaction and extracting the angular distributions of  $\Xi^-$  and  $K^+$  as well as the  $K^+\Xi^-$  and  $K^+K^+$  invariant-mass distributions [22] in addition to the total cross sections. As we have shown, these observables will certainly be very important in learning about this reaction. Also, it would be very interesting to have the beam and target asymmetries measured in future experiments. Studying the reaction channels other than  $\gamma p \rightarrow K^+K^+\Xi^-$  is also required, for these will help disentangle the isoscalar  $\Lambda$  and isovector  $\Sigma$  hyperon contributions. Theoretically, we should investigate the effects of the other higher-mass baryon resonances, not only those of the rather well-established  $J^P = 1/2^-$  and  $-3/2^+$  resonances that have been neglected in the present study but, especially, those of higher-spin (spin-5/2 and -7/2) resonances (cf. Table I). Furthermore, in future works, one should investigate the  $K\Xi$  final-state interaction and other effects mentioned in the Introduction which were not considered in the present study due to the present lack of detailed information about the relevant reaction dynamics. Evidently, the production of  $\Xi(1530)$  should be considered as a next step in the cascade spectroscopy program.

#### Acknowledgments

We are indebted to L. Guo, D. P. Weygand, and the CLAS Collaboration for providing us with the preliminary data on  $\gamma p \rightarrow K^+K^+\Xi^-$ . We also thank L. Guo, D. P. Weygand, J. Price, and T.-S. H. Lee for many fruitful discussions. This work was supported in part by the COSY Grant No. 41445282 (COSY-58).



## APPENDIX

The interaction Lagrangians used to construct our model for the production amplitudes shown in Fig. 1 are given in this Appendix. For further convenience, we define the operators

$$\hat{\Gamma}^{(+)} = \gamma_5 \quad \text{and} \quad \hat{\Gamma}^{(-)} = 1. \quad (\text{A.1})$$

The following Lagrangians describe the hadronic vertices:

*BYK Lagrangian* ( $B = \text{spin-1/2 baryon}$ ,  $Y = \text{spin-1/2 hyperon}$ ):

$$\begin{aligned} \mathcal{L}_{BYK}^{(\pm)} &= \mp g_{BYK} \\ &\times \left[ i\lambda \bar{K} \bar{Y} \hat{\Gamma}^{(\pm)} + \frac{1-\lambda}{m_Y \pm m_B} (\partial_\mu \bar{K}) \bar{Y} \hat{\Gamma}^{(\pm)} \gamma^\mu \right] B \\ &+ \text{H. c.}, \end{aligned} \quad (\text{A.2})$$

where  $B$ ,  $Y$ , and  $K$  stand for the baryon, hyperon, and kaon fields, respectively. The upper and lower signs refer to whether  $B$  and  $Y$  have the same parity (+) or the opposite parity (-). The masses  $m_Y$  and  $m_B$  are those of the hyperon  $Y$  and baryon  $B$ , respectively, and the psv mixing parameter is denoted by  $\lambda$ . For an isovector hyperon,  $\bar{Y} \rightarrow \bar{\mathbf{Y}} \cdot \boldsymbol{\tau}$  ( $Y \rightarrow \boldsymbol{\tau} \cdot \mathbf{Y}$ ) if  $B$  is an isospin-1/2 baryon. If  $B$  is an isospin-3/2 baryon instead,  $\bar{Y} \rightarrow \bar{\mathbf{Y}} \cdot \mathbf{T}^\dagger$  ( $Y \rightarrow \mathbf{T} \cdot \mathbf{Y}$ ), where  $\mathbf{T}$  is the isospin transition operator whose definition may be found elsewhere, e.g., in Ref. [13].

*BYK\* Lagrangian* ( $B = \text{spin-1/2 baryon}$ ,  $Y = \text{spin-1/2 hyperon}$ ):

$$\begin{aligned} \mathcal{L}_{BYK^*}^{(\pm)} &= -g_{BYK^*} \bar{B} \hat{\Gamma}^{(\mp)} \\ &\times \left( \gamma^\mu Y K_\mu^* - \frac{\kappa_{BYK^*}}{m_N} \sigma^{\mu\nu} Y \partial_\nu K_\mu^* \right) + \text{H. c.} \end{aligned} \quad (\text{A.3})$$

*BYK Lagrangian* ( $B = \text{spin-1/2 baryon}$ ,  $Y = \text{spin-3/2 hyperon}$ ):

$$\mathcal{L}_{BYK}^{(\pm)} = \frac{f_{BYK}}{m_K} (\partial^\nu \bar{K}) \bar{Y}_\nu \hat{\Gamma}^{(\pm)} B + \text{H. c.}, \quad (\text{A.4})$$

where  $m_K$  stands for the kaon mass.

*BYK\* Lagrangian* ( $B = \text{spin-1/2 baryon}$ ,  $Y = \text{spin-3/2 hyperon}$ ):

$$\begin{aligned} \mathcal{L}_{BYK^*}^{(\pm)} &= i \frac{g_{BYK^*}^{(1)}}{2m_N} \bar{F}^{\mu\nu} \bar{Y}_\nu \gamma_\mu \hat{\Gamma}^{(\pm)} B \\ &- \frac{g_{BYK^*}^{(2)}}{(2m_N)^2} \bar{F}^{\mu\nu} (\partial_\mu \bar{Y}_\nu) \hat{\Gamma}^{(\pm)} B + \text{H. c.}, \end{aligned} \quad (\text{A.5})$$

where  $\bar{F}^{\mu\nu} = \partial^\mu \bar{K}^{*\nu} - \partial^\nu \bar{K}^{*\mu}$  and  $m_N$  is the nucleon mass.

*BYK Lagrangian* ( $B = \text{spin-3/2 baryon}$ ,  $Y = \text{spin-3/2 hyperon}$ ):

$$\mathcal{L}_{BYK}^{(\pm)} = \frac{f_{BYK}}{m_K} \bar{B}^\nu \gamma_\mu \gamma_5 Y_\nu \partial^\mu K + \text{H. c.} \quad (\text{A.6})$$

The electromagnetic vertices are derived from the following Lagrangian densities.

*BB $\gamma$  Lagrangian* ( $B = \text{spin-1/2 baryon}$ ):

$$\mathcal{L}_{BB\gamma} = -\bar{B} \left[ \left( e_B \gamma^\mu - e \kappa_B \frac{\sigma^{\mu\nu} \partial_\nu}{2m_N} \right) A_\mu \right] B, \quad (\text{A.7})$$

where  $A_\mu$  stands for the photon field and  $e_B$  is the charge operator of the baryon while  $e$  stands for the elementary charge unit. The baryon's anomalous magnetic moment is given by  $\kappa_B$  in units of nuclear magneton.

*YY' $\gamma$  transition Lagrangian* ( $Y = \text{spin-1/2 hyperon}$ ,  $Y' = \text{spin-1/2 hyperon}$ ):

$$\mathcal{L}_{YY'\gamma}^{(\pm)} = e \frac{\kappa_{YY'\gamma}}{2m_N} \bar{Y}' \hat{\Gamma}^{(\mp)} \sigma_{\mu\nu} (\partial^\nu A^\mu) Y + \text{H. c.} \quad (\text{A.8})$$

*YY' $\gamma$  Lagrangian* ( $Y = \text{spin-1/2 hyperon}$ ,  $Y' = \text{spin-3/2 hyperon}$ ):

$$\begin{aligned} \mathcal{L}_{BY\gamma}^{(\pm)} &= i \frac{eg_1}{2m_N} A^{\mu\nu} \bar{Y}'_\nu \gamma_\mu \hat{\Gamma}^{(\pm)} Y \\ &- \frac{eg_2}{(2m_N)^2} A^{\mu\nu} (\partial_\mu \bar{Y}'_\nu) \hat{\Gamma}^{(\pm)} Y + \text{H. c.}, \end{aligned} \quad (\text{A.9})$$

where  $A^{\mu\nu} = \partial^\mu A^\nu - \partial^\nu A^\mu$ .

*BB $\gamma$  Lagrangian* ( $B = \text{spin-3/2 baryon}$ ):

$$\begin{aligned} \mathcal{L}_{BB\gamma} &= \bar{B}^\mu e_B \gamma_\alpha \left\{ g_{\mu\nu} - \frac{1}{2} (\gamma_\mu \gamma_\nu + \gamma_\nu \gamma_\mu) \right\} A^\alpha B^\nu \\ &- e \bar{B}^\mu \kappa_B \frac{\sigma^{\alpha\nu} (\partial_\nu A_\alpha)}{2m_N} B_\mu. \end{aligned} \quad (\text{A.10})$$

*BYK $\gamma$  Lagrangian* ( $B = \text{spin-1/2 baryon}$ ;  $Y = \text{spin-1/2 hyperon}$ ):

$$\begin{aligned} \mathcal{L}_{BYK\gamma} &= -eg_{BYK} \frac{1-\lambda}{m_Y \pm m_B} K (\mathbf{I} \times \bar{\mathbf{Y}})_3 \hat{\Gamma}^{(\pm)} \gamma_\mu A^\mu B \\ &+ \text{H. c.}, \end{aligned} \quad (\text{A.11})$$

where  $\mathbf{I} = \boldsymbol{\tau}$  or  $\mathbf{T}$  if  $B$  is an isospin-1/2 or -3/2 baryon.

*BYK $\gamma$  Lagrangian* ( $B = \text{spin-1/2 baryon}$ ;  $Y = \text{spin-3/2 hyperon}$ ):

$$\mathcal{L}_{BYK\gamma} = -e \frac{f_{BYK}}{m_K} K (\bar{\mathbf{Y}}^\mu \times \mathbf{I}^\dagger)_3 A^\mu B + \text{H. c.} \quad (\text{A.12})$$

In addition, the  $KK\gamma$  and  $KK^*\gamma$  interactions are

$$\mathcal{L}_{KK\gamma} = ie (K^- (\partial_\mu K^+) - (\partial_\mu K^-) K^+) A^\mu, \quad (\text{A.13})$$



and

$$\begin{aligned}\mathcal{L}_{KK^*\gamma} = & e \frac{g_{KK^*\gamma}^0}{m_K} \varepsilon^{\mu\nu\alpha\beta} \partial_\mu A_\nu \\ & \times \left[ (\partial_\alpha K_\beta^{*0}) \bar{K}^0 + (\partial_\alpha \bar{K}_\beta^{*0}) K^0 \right] \\ & + e \frac{g_{KK^*\gamma}^c}{m_K} \varepsilon^{\mu\nu\alpha\beta} \partial_\mu A_\nu \\ & \times \left[ (\partial_\alpha K_\beta^{*-}) K^+ + (\partial_\alpha K_\beta^{*+}) K^- \right],\end{aligned}\quad (\text{A.14})$$

respectively.

The coupling constants in the above interaction Lagrangians are given in Tables II and III. We use the propagators for spin-1/2 and 3/2 resonances introduced in Ref. [23], which are consistent with the above interaction Lagrangians and the Ward-Takahashi identity. Specifically, the propagator for a spin-1/2 resonance, with mass  $m_R$  and width  $\Gamma$ , reads

$$S_{1/2}(p) = \frac{1}{\not{p} - m_R + \frac{i}{2}\Gamma}, \quad (\text{A.15})$$

and that for a spin-3/2 resonance is

$$S_{3/2}(p) = \left[ (\not{p} - m_R) g - i \frac{\Delta}{2} \Gamma \right]^{-1} \Delta, \quad (\text{A.16})$$

where all indices are suppressed. Here,  $g \equiv g^{\mu\nu}$  is the metric tensor and

$$\Delta \equiv \Delta^{\mu\nu} = -g^{\mu\nu} + \frac{1}{3} \gamma^\mu \gamma^\nu + \frac{2}{3} \frac{p^\mu p^\nu}{m_R^2} + \frac{(\gamma^\mu p^\nu - p^\mu \gamma^\nu)}{3m_R}. \quad (\text{A.17})$$

The pseudoscalar and vector meson propagators are

$$\begin{aligned}\Delta_0(q) &= (q^2 - m_p^2)^{-1}, \\ \Delta^{\mu\nu}(q) &= \left( \frac{-g^{\mu\nu} + q^\mu q^\nu / m_v^2}{q^2 - m_v^2} \right),\end{aligned}\quad (\text{A.18})$$

respectively, where  $m_p$  denotes the mass of the pseudoscalar meson and  $m_v$  the vector meson mass.

Our model contains form factors at the hadronic and electromagnetic vertices to account for the composite nature of the hadrons. Currently, no theory is available to calculate these form factors from more basic principles. Here, they are introduced phenomenologically. We use the separable form for the form factor at the baryon-baryon-meson vertex,

$$F(p'^2, p^2, q^2) = f_B(p'^2) f_B(p^2) f_M(q^2), \quad (\text{A.19})$$

where  $p'^2$  and  $p^2$  denote the momentum of the outgoing and incoming baryon, respectively, and,  $q^2$  is the momentum of the meson at the hadronic vertex. The function  $f_B$  is given by

$$f_B(p^2) = \left( \frac{n \Lambda_B^4}{n \Lambda_B^4 + (p^2 - m_B^2)^2} \right)^n, \quad (\text{A.20})$$

where  $m_B$  denotes the mass of the baryon. The cutoff parameter  $\Lambda_B$  and  $n$  are kept the same for all the baryons in order to minimize the number of parameters and they are treated as free parameters to be adjusted. The above form of the form factor reduces to a Gaussian function with a width  $\Lambda_B$  in the limit of  $n \rightarrow \infty$ . The function  $f_M$  is given by

$$\begin{aligned}f_K(q^2) &= \frac{\Lambda_K^2 - m_K^2}{\Lambda_K^2 - q^2}, \\ f_{K^*}(q^2) &= \exp \left( \frac{q^2 - m_{K^*}^2}{\Lambda_{K^*}^2} \right),\end{aligned}\quad (\text{A.21})$$

for pseudoscalar ( $M = K$ ) and vector ( $M = K^*$ ) meson, respectively. Here, the cutoff parameters are fixed to be  $\Lambda_K = 1300$  MeV and  $\Lambda_{K^*} = 1000$  MeV.<sup>9</sup> The Gaussian form factor for the vector meson  $K^*$  is motivated by the work of Ref. [24], where the same form has been employed in a three-dimensional approach. However, other forms such as the dipole form factor can be employed as well without changing the results qualitatively.

Keeping gauge invariance of the reaction amplitude is not a trivial task when phenomenological hadronic form factors are present. Here, gauge invariance is maintained through phenomenological contact currents [diagrams (f) and (g) in Fig. 1] based on the Ward-Takahashi identity by extending the method of Ref. [25] for one-meson photoproduction to two-meson photoproduction processes. Explicitly, they are given by

$$C_1^\mu = \Gamma_{c1}^\mu (e_i \tilde{R}_{s1} - e_B \tilde{R}_1) + \Gamma_1 \tilde{C}_1^\mu, \quad (\text{A.22})$$

where

$$\begin{aligned}\tilde{C}_1^\mu &= -e_1 \frac{(2q_1 - k)^\mu}{t_1 - q_1^2} (\tilde{R}_{t1} - \hat{F}_1) \\ &\quad - e_i \frac{(2p + k)^\mu}{s_1 - p^2} (\tilde{R}_{s1} - \hat{F}_1) \\ &\quad - e_B \frac{(2p - 2q_1 + k)^\mu}{u_1 - s_2} (\tilde{R}_1 - \hat{F}_1),\end{aligned}\quad (\text{A.23})$$

with

$$\hat{F}_1 = \hat{R}_1 + \frac{1}{\hat{R}_1^2} (\delta_1 \tilde{R}_{t1} - \hat{R}_1) (\delta_i \tilde{R}_{s1} - \hat{R}_1) (\delta_B \tilde{R}_1 - \hat{R}_1) \quad (\text{A.24})$$

(which corresponds to an off-shell generalization of Ref. [26]) and

$$C_2^\mu = \Gamma_{c2}^\mu (e_B \tilde{R}_2 - e_f \tilde{R}_{u2}) + \Gamma_2 \tilde{C}_2^\mu, \quad (\text{A.25})$$

<sup>9</sup> We have explored the sensitivity of the results to the cutoff parameters  $\Lambda_M$  ( $M = K, K^*$ ) and found that they are not as sensitive as to the parameters  $(\Lambda_B, n)$  of the baryonic form factor.

where

$$\begin{aligned}\tilde{C}_2^\mu = & -e_2 \frac{(2q_2 - k)^\mu}{t_2 - q_2^2} (\tilde{R}_{t_2} - \hat{F}_2) \\ & - e_f \frac{(2p' + k)^\mu}{u_2 - p'^2} (\tilde{R}_{u_2} - \hat{F}_2) \\ & - e_B \frac{(2p' - 2q_2 + k)^\mu}{s_2 - u_1} (\tilde{R}_2 - \hat{F}_2),\end{aligned}\quad (\text{A.26})$$

with

$$\hat{F}_2 = \hat{R}_2 + \frac{1}{\hat{R}_2^2} (\delta_2 \tilde{R}_{t_2} - \hat{R}_2) (\delta_f \tilde{R}_{u_2} - \hat{R}_2) (\delta_B \tilde{R}_2 - \hat{R}_2). \quad (\text{A.27})$$

In Eq. (A.22),  $\Gamma_{c1}^\mu$  and  $\Gamma_1$  denote the bare  $NYK\gamma$  and  $NYK$  vertex, respectively. Likewise, in Eq. (A.25),  $\Gamma_{c2}^\mu$  and  $\Gamma_2$  denote the bare  $\Xi YK\gamma$  and  $\Xi YK$  vertex, respectively. They are obtained from the interaction Lagrangians Eqs. (A.2) and (A.11) for spin-1/2 hyperons and Eqs. (A.4) and (A.12) for spin-3/2 hyperons. Here,  $e_i$ ,  $e_f$ ,  $e_1$ , and  $e_2$  denote the combined charge-isospin operators of the nucleon in the initial state, cascade, and the kaons 1 and 2 in the final state, respectively, and  $e_B = e_f + e_2 = e_i - e_1$ . (Up to an isospin-dependent factor, the  $e_x$  are effectively the charges of the respective particles; see Ref. [25] for details.) For non-zero charges

$e_x$ , one has  $\delta_x = 1$ , and zero otherwise.  $\hat{R}$ 's and  $\tilde{R}$ 's in the above equations are hadronic form factors given by Eq. (A.19) in different kinematics. We have

$$\hat{R}_1 = F(s_2, p^2, q_1^2), \quad \hat{R}_2 = F(p'^2, u_1, q_2^2), \quad (\text{A.28})$$

and

$$\begin{aligned}\tilde{R}_1 &= F(u_1, p^2, q_1^2), \quad \tilde{R}_2 = F(p'^2, u_1, q_2^2), \\ \tilde{R}_{s_1} &= F(s_2, s_1, q_1^2), \quad \tilde{R}_{u_2} = F(u_2, u_1, q_2^2), \\ \tilde{R}_{t_1} &= F(s_2, p^2, t_1), \quad \tilde{R}_{t_2} = F(p'^2, u_1, t_2),\end{aligned}\quad (\text{A.29})$$

with

$$\begin{aligned}s_1 &= (p + k)^2, & s_2 &= (p' + q_2)^2, \\ u_1 &= (p - q_1)^2, & u_2 &= (p' - k)^2, \\ t_1 &= (q_1 - k)^2, & t_2 &= (q_2 - k)^2.\end{aligned}\quad (\text{A.30})$$

Here,  $k$  and  $p$  stand for the momenta of the photon and nucleon in the initial state, while  $q_1$ ,  $q_2$  and  $p'$ , for the momenta of the two kaons and cascade in the final state, respectively (see Fig. 1). A detailed derivation of these contact currents will be reported elsewhere [27].

- 
- [1] N. P. Samios, M. Goldberg, and B. T. Meadows, *Rev. Mod. Phys.* **46**, 49 (1974); K.-T. Chao, N. Isgur, and G. Karl, *Phys. Rev. D* **23**, 155 (1981).
  - [2] Particle Data Group, S. Eidelman *et al.*, *Phys. Lett.* **B592**, 1 (2004).
  - [3] For example, C. M. Jenkins *et al.*, *Phys. Rev. Lett.* **51**, 951 (1983).
  - [4] WA89 Collaboration, M. I. Adamovich *et al.*, *Eur. Phys. J. C* **5**, 621 (1998); **11**, 271 (1999).
  - [5] J. W. Price, J. Ducote, and B. M. K. Nefkens, in *Proceedings of the "Baryons 2002"*, edited by C. Carlson and B. Mecking, (World Scientific, Singapore, 2003), p.498.
  - [6] J. W. Price, J. Ducote, J. Götze, and B. M. K. Nefkens for CLAS Collaboration, *Nucl. Phys.* **A754**, 272c (2005).
  - [7] CLAS Collaboration, J. W. Price *et al.*, *Phys. Rev. C* **71**, 058201 (2005).
  - [8] Tagged Photon Spectrometer Collaboration, R. G. Kennett *et al.*, *Nucl. Phys.* **B282**, 626 (1987).
  - [9] L. Guo and D. P. Weygand for CLAS Collaboration, in *Proceedings of the International Workshop on the Physics of Excited Baryons (NSTAR'05)*, Tallahassee, Florida, Oct. 2005, hep-ex/0601011.
  - [10] NA49 Collaboration, C. Alt *et al.*, *Phys. Rev. Lett.* **92**, 042003 (2004).
  - [11] H. G. Fischer and S. Wenig, *Eur. Phys. J. C* **37**, 133 (2004); WA89 Collaboration, M. I. Adamovich *et al.*, *Phys. Rev. C* **70**, 022201 (2004); HERA-B Collaboration, K. T. Knöpfle *et al.*, *J. Phys. G* **30**, S1363 (2004); ZEUS Collaboration, S. Chekanov *et al.*, *Phys. Lett.* **B610**, 212 (2005); COMPASS Collaboration, E. S. Ageev *et al.*, *Eur. Phys. J. C* **41**, 469 (2005).
  - [12] W. Liu and C. M. Ko, *Phys. Rev. C* **69**, 045204 (2004).
  - [13] Y. Oh, K. Nakayama, and T.-S. H. Lee, *Phys. Rep.* **423**, 49 (2006).
  - [14] J. J. de Swart, *Rev. Mod. Phys.* **35**, 916 (1963); **37**, 326(E) (1965).
  - [15] V. G. J. Stoks and Th. A. Rijken, *Phys. Rev. C* **59**, 3009 (1999).
  - [16] C. L. Schat, N. N. Scoccola, and C. Gobbi, *Nucl. Phys.* **A585**, 627 (1995).
  - [17] D. Jido, A. Hosaka, J. C. Nacher, E. Oset, and A. Ramos, *Phys. Rev. C* **66**, 025203 (2002).
  - [18] D. B. Lichtenberg, *Phys. Rev. D* **15**, 345 (1977).
  - [19] J. W. Darewych, M. Horbatsch, and R. Koniuk, *Phys. Rev. D* **28**, 1125 (1983).
  - [20] CLAS Collaboration, S. Taylor *et al.*, *Phys. Rev. C* **71**, 054609 (2005).
  - [21] G. Wagner, A. J. Buchmann, and A. Faessler, *Phys. Rev. C* **58**, 1745 (1998).
  - [22] L. Guo and D. P. Weygand, private communication.
  - [23] K. Nakayama and H. Haberzettl, *Phys. Rev. C* **73**, 045211 (2006).
  - [24] P. M. M. Maessen, Th. A. Rijken, and J. J. de Swart, *Phys. Rev. C* **40**, 2226 (1989); Th. A. Rijken, V. G. J. Stoks, and Y. Yamamoto, *ibid.* **59**, 21 (1999).
  - [25] H. Haberzettl, *Phys. Rev. C* **56**, 2041 (1997); H. Haberzettl, C. Bennhold, T. Mart, and T. Feuster, *ibid.* **58**, R40 (1998).
  - [26] R. M. Davidson and R. Workman, *Phys. Rev. C* **63**, 025210 (2001).
  - [27] H. Haberzettl and K. Nakayama, in preparation.